Geophys. J. Int. (1989) **98**, 107–130

Numerical modelling of SH L_g waves in and near continental margins

J. Regan
Geological Survey of Canada, 1 Observatory Crescent, Ottawa, Ontario, Canada K1A 0Y3

D. G. Harkrider
Seismological Laboratory 252-21, California Institute of Technology, Pasadena, CA 91125, USA

Accepted 1989 January 11. Received 1988 December 21; in original form 1988 June 27.

SUMMARY

The effect of transition regions between continental and oceanic structures on the propagation of L_g waves from continental sources is examined. In particular, the attenuation due to variations in layer thickness in such transition regions is calculated and explained for a suite of simple models. The measured attenuation, due to the geometry of the transition regions between the oceanic and continental structures within a partially oceanic path with source and receiver in a continental structure, is at most a factor of four for frequencies from 0.01 to 1 Hz. This is inadequate to explain the observed extinction of L_g along such paths. This extinction has previously been attributed to the effects of the transition region geometry. The method used to calculate the results presented in this study is developed and its validity and accuracy are demonstrated. Propagator matrix seismograms are coupled into a Finite Element calculation to produce hybrid teleseismic SH mode sum seismograms. These hybrid synthetics can be determined for paths including any regional transition zone or other heterogeneity that exists as part of a longer, mostly plane-layered, path. Numerical results presented for a suite of transition models show distinct trends in each of the regions through which the wavefield passes. The wavefield passes through a continent–ocean transition region, then a region of oceanic structure, and finally through an ocean–continent transition region. When an L_g wavefront passes through a continent–ocean transition, the amplitude and coda duration of the L_g wave at the surface both increase. At the same time, much of the modal L_g energy previously trapped in the continental crust is able to escape from the lower crust into the subcrustal layers as body waves. The magnitude of both these effects increases as the length of the transition region increases. When the wavefront passes through the region of oceanic structure further energy escapes from the crustal layer, and produces a decrease in L_g amplitude at the surface. The rate of amplitude decrease is maximum near the transition region and decreases with distance from it. When the wavefield passes through the ocean–continent transition region a rapid decrease in the L_g amplitude at the surface of the crust results. The energy previously trapped in the oceanic crustal layer spreads throughout the thickening crustal layer. Some of the body wave phases produced when the wavefield passes through the continent–ocean transition region are incident on the continental crust in the ocean–continent transition region. These waves are predominantly transmitted back into the crust. The other body wave phases reach depths below the depth of the base of the continental crust before reaching the ocean–continent transition and, thus, escape from the system.

Key words: synthetic seismograms, L_g waves, continental margins, finite element, attenuation

INTRODUCTION

This paper presents a study of the propagation of L_g waves across ocean–continent transition regions. The transition regions are represented by simplified models each consisting of a crustal layer with a smoothly varying thickness above a half-space. The wavefields transmitted through the transition region models are calculated to model L_g. The modal interpretation of L_g on which the calculation of synthetic seismograms is based will be justified below. The importance of the method introduced in the next paragraph and its application to studies of L_g propagation in major

areas of study such as tectonic mapping and nuclear discrimination will be explained, and the new results this method will make possible will be discussed and related to previous work.

The changes to a L_g wavefield, as it travels across a transition region, are modelled using a hybrid method which combines the Finite Element method (FE) and the Propagator Matrix technique (PM) (Harkrider 1964, 1970, 1981). PM seismograms for L_g waves from a continental source are coupled into a FE calculation which propagates the L_g wavefield across the continent–ocean boundary. Results from the FE calculation are then coupled into a second FE calculation which propagates the L_g wavefield through an ocean to continent transition region. The results of either FE calculation may be propagated through a region of horizontally uniform waveguide by coupling them back into a PM calculation using the Seismic Representation theorem (RT) (de Hoop 1958). The FE to PM coupling can be used to economically investigate the effects of long ocean path lengths between regions and is the subject of later papers. Here we restrict ourselves to regions in and near transition zones separated by short ($\leq$150 km) ocean paths.

One of the important types of observational studies of L_g has been to distinguish regions with oceanic crustal structures from those with continental crustal structures. Press & Ewing (1952) and Bath (1954) observed extinction of L_g when the propagation path included an oceanic portion of length greater than 200 km, and high attenuation or extinction when the oceanic path length was as short as 100 km. This led to the commonly used assumption that paths which pass under oceans but do not attenuate L_g are continental. The results of the present paper seriously challenge the interpretation that paths with short oceanic portions which show little or no L_g attenuation are necessarily continental. They may necessitate the reassessment of some of the results of studies of L_g in many regions of the world (Press, Ewing & Oliver 1956; Savarensky & Valdner 1960; Bolt 1957; Lehmann 1952, 1957; Oliver, Ewing & Press 1955; Herrin & Minton 1960; Wetmiller 1974; Gregersen 1984; Kennett & Mykkeltveit 1984).

Another major use of L_g waves is in the determination of magnitudes, m_{bL_g}, of explosions and earthquakes. Different types of magnitudes, including m_{bL_g}, are compared to discriminate between the two types of sources (Blandford 1982; Pomeroy, Best & McKevilly 1982). m_{bL_g} measurements are also used to derive γ, the coefficient of anelastic attenuation, which is important in many types of wave propagation and attenuation studies and can be employed to assess the possible destructiveness of earthquakes. It is important to understand if reflections, refractions, or diffractions from changes in crustal thickness, generally ignored in studies measuring m_{bL_g} or γ will produce significant effects not accounted for in the interpretations given (Nuttli 1973, 1978, 1981; Herrmann & Nuttli 1975, 1982; Street 1976, 1984; Street, Herrmann & Nuttli 1975; Street & Turcotte 1977; Jones, Long & McKee 1977; Bollinger 1979; Barker, Der & Mrazek 1981; Nicolas *et al.*, 1982; Dwyer, Herrmann & Nuttli 1983; Chung & Bernreuter 1981; Singh & Herrmann 1983; Campillo, Bouchon & Massinon 1984; Herrmann & Kijko 1983).

The preferred interpretation of L_g is in terms of a superposition of higher mode surface waves. This higher mode surface wave interpretation of L_g was initially unpopular because, in its earliest forms, based on fundamental mode Love waves alone, it did not explain the vertical and longitudinal components and the long coda. However, it subsequently superseded the alternate explanation in terms of channel waves trapped in the crust above a low-velocity layer for the following reasons. Oliver & Ewing (1957, 1958), Oliver, Dorman & Sutton (1959) and Kovach & Anderson (1964) showed that all components of L_g could be interpreted by considering both higher mode Rayleigh and Love waves. Knopoff *et al.* (1975), Panza & Calcagnile (1974, 1975) and Bouchon (1981, 1982) used the higher mode interpretation of L_g to calculate synthetic seismograms, which demonstrate that a low-velocity channel below the crustal waveguide was unnecessary. Other phases previously defined in terms of the channel model have been successfully modelled using the higher mode surface wave model. Schwab, Kausel & Knopoff (1974) and Mantovani *et al.* (1977), considered S_a, Panza & Calcagnile (1975) considered R_g and L_i, and Stephens & Isacks (1977) considered the transverse component of S_n. Clearly, the multimode surface wave explanation of L_g is valid and useful. However, the long L_g coda observed is still not completely understood for phase velocities less than 2.8 km s^{-1}. The attribution of this long coda to diffraction and reflection from crustal structure is supported by the results presented in this study.

A simple parallel of the multimode surface wave interpretation, which is a very useful aid in the interpretation of the wavefields presented in this study, is the representation of the multimode L_g arrivals as superpositions of multiply reflected post-critical SH and SV rays trapped in the crustal layer. Bouchon (1982) used this type of interpretation for L_g arrivals for group velocities between 3.5 and 2.8 km s^{-1}. Pec (1967) and Kennett (1986) also used the ray approach to address properties of L_g. This type of interpretation can also be used to explain where structure causes conversions from L_g to distinct body waves or from one SH mode to another. Gregersen (1978) discusses conversion between different modes of Love waves and between Love and Rayleigh waves at ocean–continent boundaries. For near normal incidence conversion between Love and Rayleigh waves is shown to be a small effect. However, future 3-D modelling would be necessary to confirm these conclusions based on an approximate method. Understanding conversion between modes of L_g and between L_g and other phases is an important part of understanding the mechanisms of attenuation of L_g along mixed paths.

Many attempts to understand the propagation of seismic disturbances across regions of varying structure such as transition zones have been made. First, simple models were used and analytical solutions were derived for soluble special cases, then increasingly complicated models were considered as available computational power increased. The types of models that have been used to approximate transition regions can be separated into several types which are illustrated in Fig. 1. Sato (1961a) derived analytical results for models of type 1a (Fig. 1a) with $L = 0$ and $L > 0$. Kennett (1973) considered the problem of seismic waves interacting with a layer or layers in which properties change across a surface perpendicular to or at a specified angle from

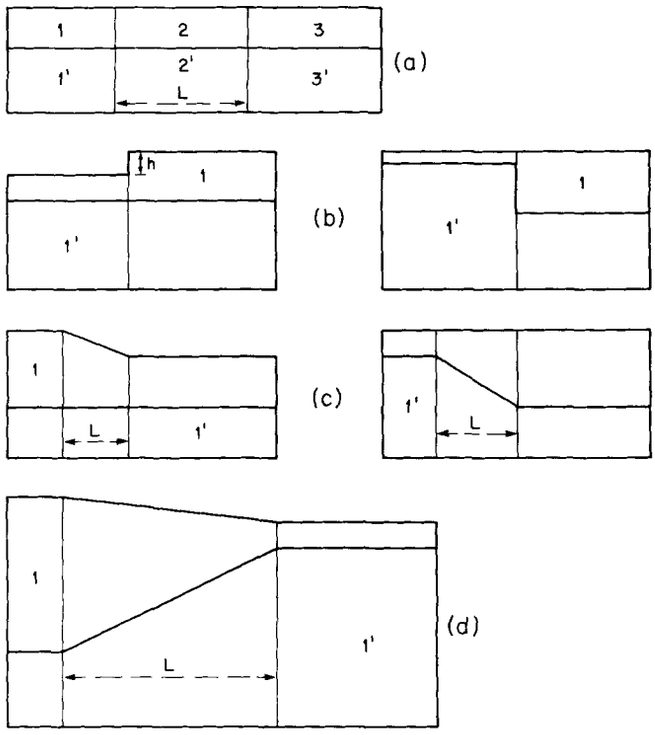

Figure 1. Types of models used in studies of propagation of Love waves across continent–ocean boundaries, in order of increasing complexity. (a) shows two homogeneous layered regions, 1 and 3, separated by an intermediate region, 2, in which elastic properties vary smoothly between their values in regions 1 and 2. (b) shows a layer over a half-space with a step change in the thickenss of the layer. (c) shows a model with a smooth change in thickness, either at the surface or the Moho. (d) shows a model with a smooth change in thickness both at the surface and the Moho. The variations in (a), (c), and (d) occur in a transition region of length L.

the layering. Several types of solutions for models of type 1b (Fig. 1b) have been derived. Sato (1961b) obtained approximate analytical reflection and transmission coefficients, for $h \ll \lambda$, where h is the crustal thickness and λ is the incident wavelength. Hudson & Knopoff (1964), Knopoff & Hudson (1964), Hudson (1977) and Bose (1975) derived similar solutions without applying the $h \ll \lambda$ constraint. Alsop (1966) developed an approximate solution for these coefficients applicable when all energy remains in Love waves. Gregersen & Alsop (1974, 1976) extended this method to the case of non-normally incident Love waves. They found that for oblique incidence at angles less than 40° normal incidence is a good approximation. Kazi (1978a, b) derives solutions that account for and demonstrate the importance of the Love waves converted to scattered body waves at the surface step. Martel (1980) used a FE technique and spatial filtering to isolate the diffracted body wave component. Many workers have studied models of type 1c (Fig. 1c). Knopoff & Mal (1967), and Knopoff *et al.* (1970) derived an analytical solution usable when the slope of the surface (or Moho) in the transition region is small. Pec (1967) calculated the dispersion of Love waves propagating in a wedge-shaped layer and found that the largest changes in phase velocity and amplitudes occur at short periods. Boore (1970) studied the propagation of a simple Love wave ($T > 20$ s), using the Finite Difference (FD) method. He noted that in the region of the transition mode conversions and conversion to other types of waves seemed to be important. Lysmer & Drake (1971, 1972) and Drake (1972) use a FE method based on Zienkiewicz & Cheung (1967). This formulation requires that the incident modal energy is exactly equal to the sum of the reflected and transmitted modal energy. The body waves present in the system produce distortions to the elastic layer over a half-space eigenfunctions, which increase for higher modes. Drake & Bolt (1980) used the same method with a model of type 1d (Fig. 1d) to study a more realistic model fitting fundamental mode phase velocity data for events normally incident on the California continental margin at periods between 4.4 and 60 s.

All the studies discussed in the previous paragraph used periods much longer than those that will be considered in the following discussions. The shorter periods used in this study allow the examination of the effects of transition regions with L many times λ. The energy escaping from the crustal waveguide is shown in this study to be an important component of the explanation of the attenuation of the L_g phase travelling on partially oceanic paths. Previous studies considered mainly fundamental mode Love wave input sampled at a selection of discrete frequencies, while the forcing functions used in this study are a sum over a range of frequencies on the fundamental and first five higher branches. Of the previous studies, only Kennett & Mykkeltveit (1984) have generated realistic seismograms similar to those used in this study; instead other studies concentrated on measuring phase velocities and transmission and reflection coefficients.

PROPAGATOR TO FINITE ELEMENT COUPLING

The hybrid method used in the present study allows the determination of synthetic L_g seismograms for propagation paths which include a non-plane-layered transition region as a small portion of a longer mostly plane-layered path. A graphical representation of the hybrid method is shown in Fig. 2. No transition region is illustrated in the figure, but any type of structure may be inserted into the FE grid. Within a plane-layered medium, that is outside any transition region, the 'trapped' wavefield can be mathematically constructed at any point receiver using the PM technique and an appropriate form of a source representation. The resulting far-field seismogram will include not only a direct arrival but also the superposition of many multiple critical and post-critical reflections which produce the surface waves in the wavetrain. Each such PM seismogram is represented in Fig. 2 by a single solid line from the source to the receiver. A set of PM seismograms, for a specified source function, are generated at a group of intermediate receivers, equally spaced in z, located at the grid edge notes of the FE grid, a horizontal distance X from the source. This type of set of seismograms will be referred to as a set of forcing functions. The depth spacing between the intermediate receivers, Δx, is also the node spacing in the FE grid of rectangular elements into which the wavefield is to be coupled. The PM forcing functions are applied as displacement time history constraints on the left-most

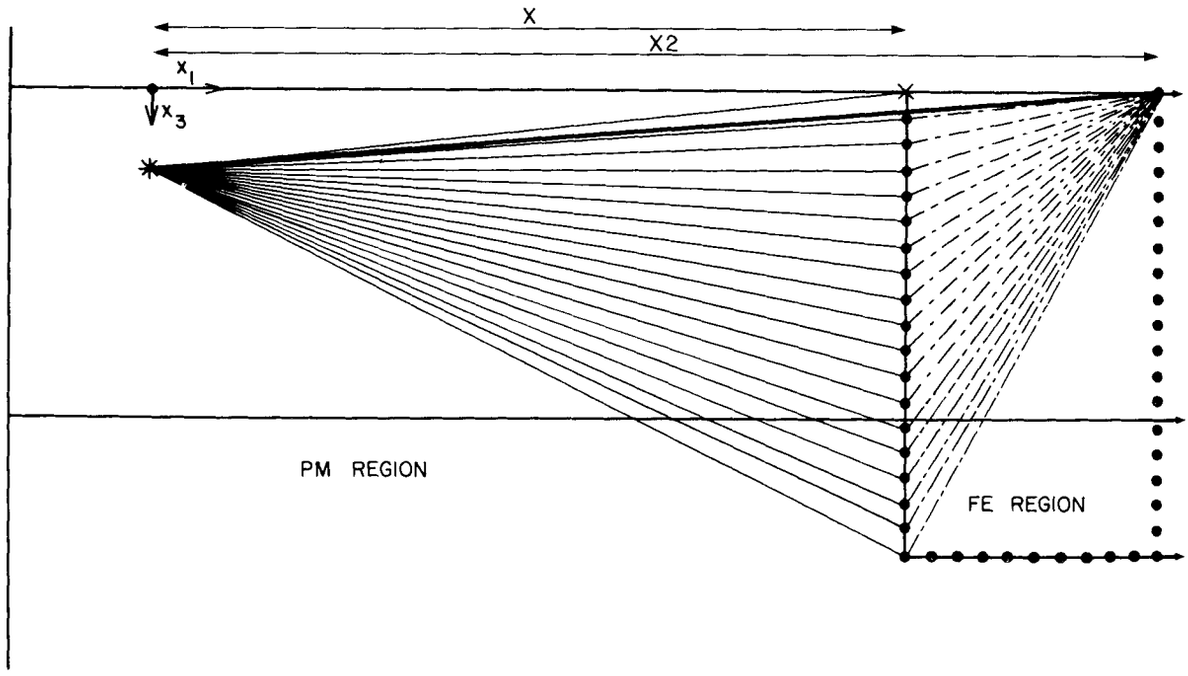

Figure 2. Geometry used to explain the coupling of PM seismograms from a source outside a FE grid into a FE grid. The two long horizontal lines show the free surface and the boundary between the layer and the half-space. The source is shown as an asterisk. Two columns of FE nodes are shown as dots. The vertical line connecting the dots and the short horizontal line perpendicular to it are grid edges. All receivers located at nodes on the left-most edge of the FE grid will be referred to as intermediate receivers. The heavy solid line from the source to the surface receiver in the grid denotes the direct analytical seismogram, the solid lines between the source and the grid edge nodes denote the direct forcing functions, and the dotted lines indicate the source to receiver paths, for the sources created by the application of the forcing functions at the grid edge. Integration over all dashed paths gives the hybrid seismogram.

column of nodes in the FE grid, thus, completely specifying the subsequent motion at all points in that FE grid. Each node to which a forcing function is applied becomes a source point in the FE calculation. Any point in the FE grid may be chosen as the receiver. The receiver is assumed to be a horizontal distance $X2$ from the source. The hybrid seismogram recorded at this receiver is a superposition of the seismograms produced by each source point along the FE grid edge. Each of these component seismograms are indicated by a dotted line in Fig. 2.

The seismograms used as forcing functions can be generated using more than one type of source. For a line source, in a homogeneous half-space or a layered half-space the applied forcing functions are $u_y(x, y, z)$. For a double couple point source the PM solutions can be expressed in cylindrical coordinates as

$$[\bar{v}(r, \phi, z)] = \bar{v}_\nu(\phi, z)\frac{\partial H_\nu^{(2)}(k_L r)}{\partial r},$$

where r is the source to receiver distance, k_L is the wavenumber of the Love wave mode being considered, $H_\nu^{(2)}(k_L r)$ is the Hankel function of the second kind, and $\bar{v}_\nu(\phi, z)$ is a factor containing all terms relating to the source and to propagation in z. 2-D and 3-D propagation show different rates of spreading with distance. The rectangular grid FE code used is based on the SWIS FE code (Frazier, Alexander & Petersen 1973), and is a 2-D Cartesian formulation. Thus, for consistency the forcing functions applied to the FE grid edge should be 2-D Cartesian results, u_y. It must be demonstrated that the application of 3-D cylindrical forcing functions to a 2-D FE grid produces hybrid seismograms that approximate the 3-D cylindrical solution $[\bar{v}(r, \phi, z)]$ at the receiver. It is demonstrated below that the discrepancies in the 3-D cylindrical hybrid solution due to the 2-D propagation in the FE portion of the path are negligible or easily corrected for.

Consider a FE grid with its leftmost edge a distance $X = r_1$ from a source, and a receiver, where hybrid and analytical synthetic results are recorded, a distance $X2 = r_2$ from the source. Define the distance propagated within the FE grid as $\Delta r = r_2 - r_1$. Since we are considering the case of r large, $k_L \gg \nu/r$, $[\bar{v}(r_2, \phi, z)]$ can be expressed in terms of r_1, ϕ, z, and Δr as

$$[\bar{v}(r_2, \phi, z)] = [\bar{v}(r_1, \phi, z)]\sqrt{\frac{r_1 + \Delta r}{r_1}}\exp(-ik_L\Delta r)$$
$$\approx [\bar{v}(r_1, \phi, z)]\exp(-ik_L\Delta r) \quad \Delta r \ll r_1 \quad k_L r_1 \gg 1.$$

Now, for a line source the analogous modal continuation relation is,

$$u_\phi(x_2, z) = u_\phi(x_1, z)\exp[-ik_L(x_2 - x_1)]$$
$$= u_\phi(x_1, z)\exp(-ik_L\Delta x).$$

Comparing, we see that both expressions have the same form. In each case the displacement at r_2 can be expressed as the displacement at r_1 multiplied by a propagation factor. A 2-D FE or RT calculation will give the same propagation factor for each mode as the analytical expression above. If the displacements at r_1, $v(r_1, \phi, z)$ or $u_y(x, z)$, and the propagation factors, $\exp(-ik_L\Delta r)$ or $\exp(-ik_L\Delta x)$, are

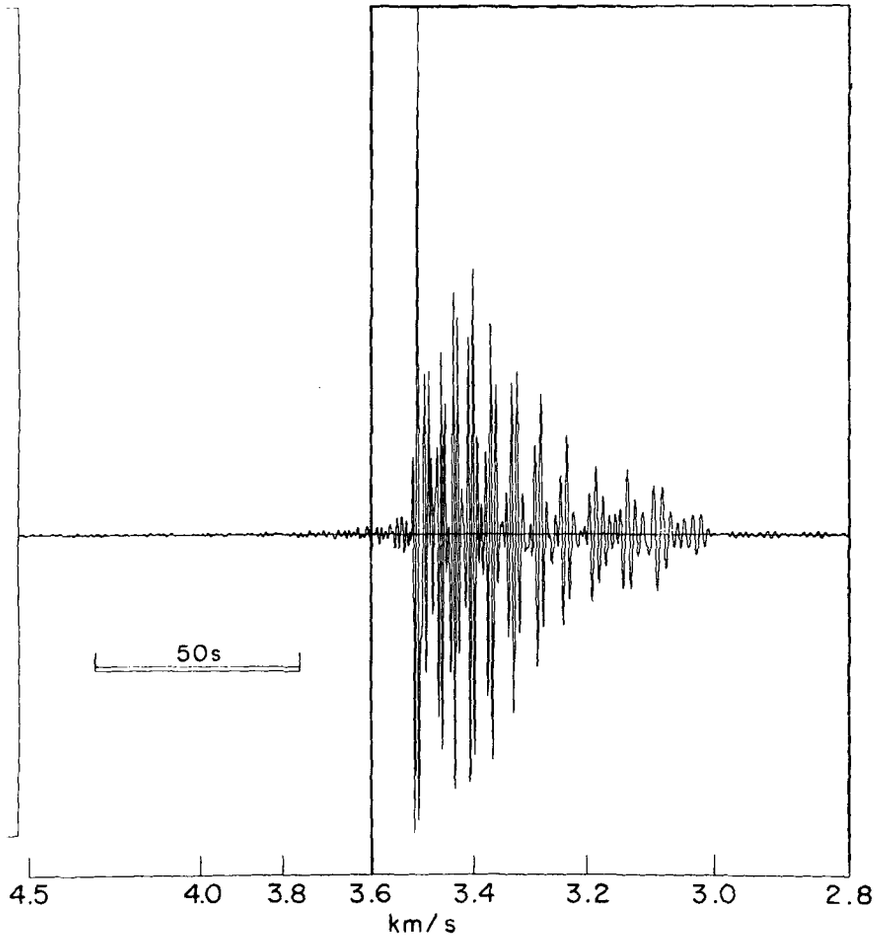

Figure 3. Sample PM mode sum synthetic seismogram for SH L_g 1500 km from the source. The seismogram includes modes with periods between 0.5 and 100 s. The fundamental and the first five higher modes are used. The seismogram has been bandpass filtered between 0.01 and 1 Hz, and has the WWSSN short period instrument response convolved with it. The box shows the time window used to select the forcing function. The numbers along the axis indicate the group velocities of the arrivals.

correlated by considering $x_1 = r_1$ and $\Delta x = \Delta r$, then $\bar{v}(r_2, \phi, z)$, the 3-D solution, will be given by $u_y(x_2, z)$, the result of the 2-D FE or RT calculation. The source must be many λs, from the boundary and r must be normal to the FE grid edge and in the plane of the FE grid.

The PM seismograms $[\bar{v}(r, \phi, z)]$ used as forcing functions in the tests discussed below show the overall character of the arrivals seen in data in the L_g group velocity range of between 2.8 and 3.5 km s^{-1} (Fig. 3). The seismograms are complete to a period of 1.9 s and contain most of the energy for periods down to 0.5 s. A triangular time function with rise time 0.2 s, and decay time 0.2 s is used. The rectangle in Fig. 3 delimits the time window used to select the portions of the seismograms used as displacement time history forcing functions. No intrinsic attenuation is included in the seismograms, since the object of this study is to determine the attenuation caused by the geometry of the layers of the earth model. The forcing functions have been filtered between 0.01 and 1 Hz using a 3-coefficient two-way minimum phase time domain bandpass filter. This removes frequencies too high to be accurately transmitted in the FE grid. The forcing functions used in subsequent calculations differ from the seismogram shown in Fig. 3 in that no instrument response has been applied. The instrument response is applied to the FE result.

DESIGNING FE GRIDS

The FE grids discussed in this section are designed to represent the two classes of transition models illustrated in Fig. 4. The difference between individual transition models within each class was L, the length of the transition region. Real ocean to continent type transitions occur over lengths of 50–300 km (Keen & Hyndman 1979; Hinz *et al.*, 1979; Eittreim & Grantz 1979; Le Douaran, Burrus & Avedik 1984). However, for the present studies, an upper limit on L of 100 km was imposed by the computation limits discussed below. The lengths used for this investigation were a step transition ($L = 0$ km), $L = 25$, 50 and 100 km.

Results in this paper were generated using a Ridge computer at Caltech and a Convex C1 computer at the GSC. The largest FE calculation was allowed up to 48 cpu hours on the Ridge. Moving to a faster machine like the Convex or a supercomputer does not allow the increases in grid length that might be expected. As the path length in the grid increases, numerical dispersion becomes a more serious

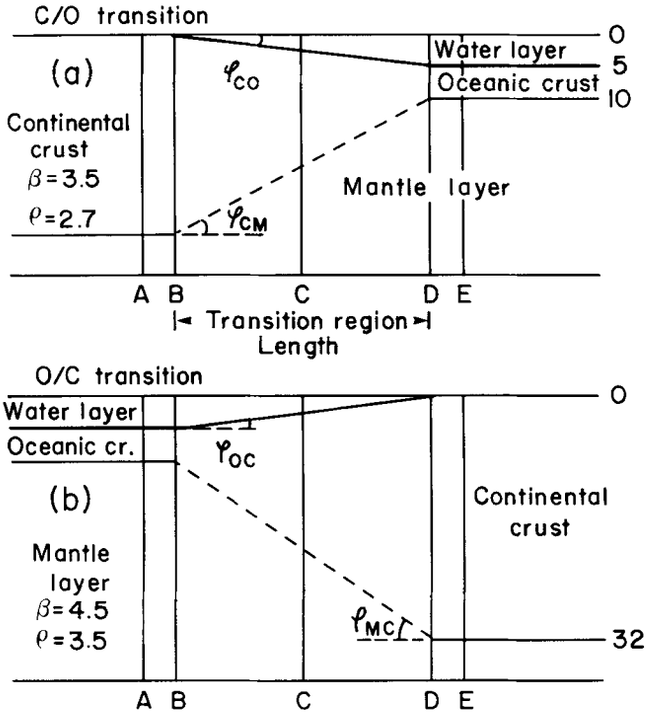

Figure 4. Explanation of terms and illustration of the model classes used to describe the behaviour on passage through a transition region. The heavy line between the water layer and the crustal layer is the surface. The sloping portion of this surface is the continent to ocean boundary (COB) for the C/O transition model and the ocean to continent boundary (OCB) for the O/C transition model. Similarly, the sloping dashed line between the crust and mantle layers is the crust to mantle boundary (CMB) for the C/O transition and the mantle to crust boundary (MCB) for the O/C case. The length of the transition, L, is the distance from B to D, B is referred to as the beginning of the transition, D as the end of the transition, C as the centre of the transition. A is 5 km from B, E is 5 km from D.

difficulty making decreases in grid spacing necessary. Also, the grid length grows 50 per cent faster than L. To obtain a significant increase in grid length a more accurate higher order FE or FD scheme would be advisable and double precision calculations might become necessary.

The first class of models used in this study describe continent to ocean transition regions. In further discussions these models will be referred to as C/O models, and the transitions they represent as C/O transitions. Similarly, the second class of models described ocean to continent transition regions, and will be referred to as O/C models. The transitions they represent will be referred to as O/C transitions. The continental reference model consists of a 32 km thick crustal layer over a half-space. The oceanic reference model consists of two 5 km layers, one water and one crust, over a half-space. Each C/O or O/C transition region is characterized by a continuous rate of thinning or thickening of the crustal layer. In all models the crustal layer has an SH wave velocity, of $3.5\,\mathrm{km\,s^{-1}}$ and a density of $2.7\,\mathrm{g\,cc^{-1}}$, while the half-space has an SH wave velocity of $4.5\,\mathrm{km\,s^{-1}}$ and a density of $3.4\,\mathrm{g\,cc^{-1}}$. Each class of transition models has the same boundary conditions (BCs) applied to each of its members. The forcing functions used to drive the C/O transition and continental reference FE calculations are a vertical section of 60 mode sum seismograms, calculated at depth intervals of 0.5 km beginning at the surface, for a strike slip source at 8 km depth at a distance $X = 1500$ km. The forcing functions for the O/C transition and oceanic reference tests are recorded during the 50 km C/O transition calculation. They consist of a depth section of hybrid seismograms recorded 25 km past the oceanic end of the 50 km C/O transition region, 1755 km from the source. The vertical spacing within the depth section is 0.5 km. All other BCs are identical for all models. The transmitting BC is applied to all edge nodes of the grid, excluding only the free surface and the nodes to which forcing functions are applied.

The first step in designing a grid for FE calculations is to determine grid spacing, dx, and the time step duration, dt. For computational efficiency it is important to maximize dx and dt. At least six nodes per wavelength (Frazier *et al.*, 1973) are needed to avoid numerical dispersion problems. To maintain numerical stability, the wavefront can travel no more than half the grid spacing per time step. Thus, dx and dt must be chosen to satisfy

$$dx \leq \frac{V_{\min}}{6f} \qquad dt \leq \frac{dx}{2V_{\max}}$$

where f is the highest frequency in the waveform to be modelled and $V_{\min}$ and $V_{\max}$ are the minimum and maximum S velocities respectively in the dominant part of the model. In this study, we are considering L_g waves with a predominant period of approximately 1 s, in a medium with $V_{\min} = 3.5\,\mathrm{km\,s^{-1}}$ and $V_{\max} = 4.5\,\mathrm{km\,s^{-1}}$. Thus, we have chosen $dx = 0.5$ km and $dt = 0.05$ s.

The next step in designing the grid is the determination of the dimensions of the grid, nx and ny, the duration of the input forcing functions, T_{mi}, the duration of the calculated time series, $T_{m\,\mathrm{calc}}$, and the location of the transition region within the grid. The vertical column of nodes at which forcing functions are applied lie at the leftmost edge of the FE grid. This column of nodes at the grid edge appears as a rigid boundary to energy incident upon it from within the grid. The criteria below, used to choose the location of the transition region within the grid, are designed to avoid contamination from reflections from the leftmost grid edge. The location of the transition region within the grid is defined in terms of the distances from the leftmost grid edge to positions A, B, C, D, E, in Fig. 4. The values of these parameters were chosen to satisfy two criteria.

(a) A seismogram of duration D_s seconds can be recorded at A (Fig. 4) before the multiple reflection of the input wave from the beginning of the transition, B, to the leftmost grid boundary and back again reaches A.

(b) A seismogram, uncontaminated by the multiple reflection, with duration D_s seconds can be recorded at the receiver closest to the right-most edge of the grid. This receiver is defined to be at a distance x_f from the left-most grid edge.

Criteria A and B concern themselves only with reflections from the left-most edge of the grid. Non-physical reflections from the bottom and the right-most edge of the grid are removed using transparent BCs which will be discussed later. The BC cannot be applied at a node constrained by a

Table 1

	nx	nz	nt	T_{mcalc}	A	B	C	D	E
model	# nodes		$\#\Delta t$	s	# nodes				
0C/O	310	90	1921	96	230	240	240	240	250
25C/O	365	90	2101	105	240	250	275	300	310
50C/O	525	90	3101	155	350	360	410	460	470
100C/O	500	90	2441	122	250	260	360	460	470
0O/C	350	90	2561	128	275	285	285	285	295
25O/C	400	90	2501	125	275	285	310	335	345
50O/C	450	90	2601	130	275	285	335	385	395
100O/C	525	90	2941	147	275	285	385	485	495
fref	530	90	3201	160					
rref	525	90	3201	160					

forcing function. The duration D_s was chosen to be 55 s, the observed coda duration for a SH L_g mode sum seismogram at a distance of 1000 km from the source. For all the models used in this study the values of parameters defining the size of the grid and the location of the transition region within it are given in Table 1. Distances are given as the number of nodes in the horizontal direction from the left edge of the grid to the depth section or boundary indicated. The model names consist of a number that indicates L, then the model type. Reference layer over half-space models are indicated by ref.

SAMPLING FE SOLUTIONS

Analysis of the effects of various transitions on the waveforms and amplitudes of L_g waves using FE techniques requires that the motions of the nodes of the FE grid be sampled so that the progress of the L_g waves across the transition can be observed. Two methods of sampling are used in this study. Complete displacement time histories are recorded for selected nodes, and the displacements of all nodes in the grid are recorded at given time intervals. The first approach produces seismograms which can be used to illustrate variations of amplitude and waveform with distance or depth, the second approach produces time slices and is a clear way to illustrate the propagation and distortion of wavefronts caused by passage through the inhomogeneous structure. Time slices are self scaled so that successive time slices may show the same absolute amplitude as a different symbol size. Thus, the same region of the waveform will appear darker on a time slice with a given maximum amplitude than on another time slice with a larger maximum amplitude. This difference must be remembered when interpreting the time slices.

The amplitude of the first large positive and negative peaks in L_g mode sum seismograms (Fig. 3) are extremely sensitive to distance from the source and to the time spacing and starting time chosen when calculating the synthetics. It is not unusual for very small changes in these parameters to produce variations in amplitude of several per cent. An improved filtering technique would reduce the variation slightly by removing more of the sampling effects due to the non-zero spectral amplitude at the Nyquist frequency. However, a significant portion of the variation is apparently due to changes in the patterns of interference between multiple arrivals. In addition, the direct S pulse and the end of the S_n wavetrain arrive at the same time as the initial pulses in the L_g wavetrain. The longer period portions of the S and S_n arrivals have been removed by the bandpass filter. However, some non-L_g energy will be present in the first few cycles of the trace. Unfortunately, the initial high frequency peaks, which are affected by the problems discussed above, yield the maximum peak to peak amplitude. This indicates that peak to peak amplitude will be a poor measure of the L_g amplitude. A more stable measure of amplitude correspondence between seismograms of this type is the rms amplitude calculated over some time window appropriate to the seismograms being compared:

$$\text{rms} = \sqrt{\frac{\sum_{n=1}^{m} [\text{amp}\,(n)^2]}{m}} \qquad m = \frac{T_{\text{rms}}}{\Delta t}$$

where m is the number of points in a sampling window of duration T_{rms} seconds. Such an rms amplitude measure will reduce the effects of S or S_n contamination and of any other instabilities affecting the initial arrivals.

The evaluation of rms amplitudes is straightforward once the sampling window has been chosen. The location of the sampling window with respect to the arrivals of maximum amplitude, and the duration of the trace contained within the sampling window, have a significant effect on the value of the rms amplitude. Care must be taken to choose windows for two sets of results that produce meaningful comparisons. When results of two separate FE calculations are being compared, at corresponding nodes, both seismograms should begin at the same absolute time. When successive seismograms in a depth or distance section, from a single calculation, are being compared, the duration of the sampled portion of the trace with negligible amplitude that occurs before the first arrival must be constant. A general approach which does not require the use of theoretical travel times was chosen to determine windows in the latter case. The first and last point in the sampling window are selected by bracketing the portion of the seismogram with significant amplitude according to the following algorithm:

(1) Set a cut-off value for the amplitude at some fraction of the maximum absolute value of amplitude in the seismogram (usually 0.01 or 0.05).

(2) Let the sample at the location of the maximum absolute value be the first sample in each of two series. One series proceeds forward in time, the other backward. Scan each series until a subseries of samples n seconds in duration, all with amplitudes smaller than the cut-off amplitude, is found. The first point in each of these subseries defines an endpoint of the seismogram.

(3) Calculate the rms amplitude for sampling windows with durations $15, 20, 25, \ldots, 85$ s. If the duration of a sampling window exceeds the duration of the seismogram then no rms amplitude is determined.

This algorithm yields a series of rms amplitude values for the selected set of windows. If rms amplitudes of the data and the synthetics agree in all windows, and waveforms are similar the fit is considered to be excellent. When trends in rms amplitude are discussed, the longest window common to all seismograms being studied will be used. If rms amplitude trends change when window length is varied these changes will be discussed since examining the behaviour of the rms amplitude as a function of sample window length can give insight into the nature of and the underlying reasons for misfit between methods.

TESTS OF ACCURACY: SH L_g MODE SUM INPUT

The BCs are introduced to remove the non-physical reflections created by the artificial grid boundaries at the ends and bottom of the grid. Removing these reflections from the portions of the seismogram of interest by extending the grid requires an increase in execution time of between 30 and 500 per cent. As a comparison, the approximate BC used in this study increases execution time by 3–5 per cent. The BC used here was suggested by Frazier *et al.* (1973). The average of the rigid boundary and the free boundary displacements for each constrained node is calculated at each time step. For a normally incident plane wave this average exactly represents the transparent boundary. However in practice the incident wavefront is neither normally incident nor a plane wave. This means that the actual value at the transparent boundary is a linear combination of the rigid boundary and free boundary solutions whose coefficients depend upon the angle of incidence of the energy. The boundary condition used here assumes that the average of the two solutions will in most cases be the best approximation to the transparent boundary that can be simply implemented.

A series of tests were conducted to verify the accuracy of the coupling method and the efficiency of the transparent BCs. The tests used the continental reference model and a set of 90 forcing functions calculated for a strike slip point double couple source at a depth of 8 km and a distance $X = 1500$ km. Transparent BCs were applied to all grid boundaries except the free surface and the nodes to which forcing functions were applied.

The results of the accuracy and BC tests presented below are illustrated in Fig. 5. A continental reference structure is used for both the FE and PM portions of the path. This allows the direct comparison of the hybrid solutions and the direct analytical synthetics calculated entirely with the PM technique. Four separate calculations were performed. First, L_g mode sum direct analytical seismograms for the same source used to generate the C/O transition forcing functions were calculated. Next, seismograms were generated using the hybrid method in a grid long enough (100×50 km) to prevent contamination from end reflections. Third, seismograms were generated using the hybrid method and a short (50×50 km) grid with the transparent BC applied at each node on its right-most edge. Finally, the previous FE calculation was repeated without the transparent BCs. The excellent agreement between the analytical and hybrid synthetics verifies the validity of the coupling method applied to a layered half-space. Small discrepancies are seen in the higher frequency component, particularly in the first 20 s of the trace. In the last trace of each group in Fig. 5 the single and multiple reflections from the grid edge are clear. Comparison of the long grid and the short grid with and without BCs shows that most of the reflected amplitude has been removed by the BCs. The misfit is lower for the longer period component of the traces. The significant misfit is coincident with reflections, and is largest for the multiple reflections. Despite visible differences in waveform the seismograms shown in Fig. 5 have rms amplitudes that agree to within less than 2 per cent for all rms window lengths. This indicates that small changes in waveform may be expected but the rms amplitudes of the seismograms should be stable and not significantly contaminated by incompletely removed reflections from the grid edges. The increased discrepancies in both waveform and amplitude introduced by the multiple reflections will be avoided in the transition FE grids described below. This reduces the discrepancies in rms amplitude to less than 1 per cent.

Reflections from the bottom edge of the grid should also be considered. The transparent BC can be very ineffective for the small angles of incidence seen at the grid bottom

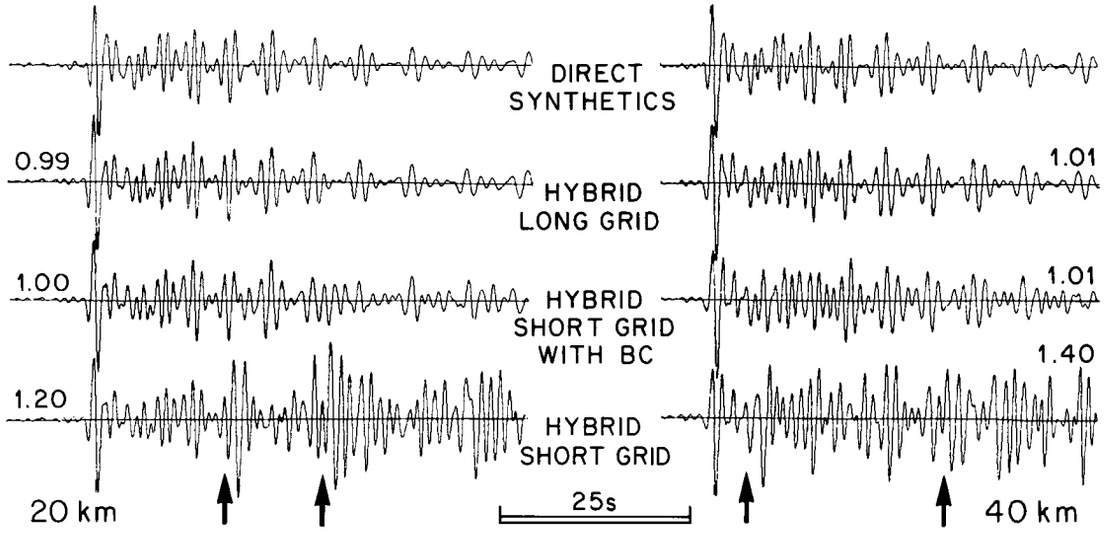

Figure 5. Seismograms recorded at the surface for $X2 = 1520$ and 1540 km. The first seismogram in each group is a direct synthetic, the second is a hybrid synthetic determined using the long grid (200×100), the third and fourth are hybrid synthetics determined using a short (100×100) grid with and without the transparent BC, respectively. When the boundary condition is applied it is applied only at the right-hand edge of the grid. The number beside each of the hybrid synthetics is the rms amplitude ratio between that hybrid seismogram and the direct synthetic. Seismograms have been bandpass filtered between 0.01 and 1 Hz and have been convolved with the short period WWSSN instrument response. Arrival times of the single and multiple reflections are indicated by the arrows below each group of seismograms.

when a distant source is considered (Regan 1987). Fortunately, in a layered half-space, where L_g waves can be modelled as the superposition of multiply reflected post-critical SH waves in the crust, most of the energy in the SH type L_g waves should be trapped in the crustal layer. The time slices discussed later (Figs 6, 12) show that the SH type L_g waves propagating in a layer over a half-space are, in the most part, confined within the layer; rms amplitudes agree to within less than 0.1 per cent with and without the transparent BCs (Regan 1987). However, the purpose of the present study is to examine the effects of continental–oceanic boundaries on the transmission of L_g mode sum seismograms. When the crustal layer is thinned or thickened with distance, the modes are no longer completely trapped within the layer. Energy can be converted to modes compatible with the local layer thickness and to other forms including body waves that can propagate into the half-space. When the wavefield reaches the second layered structure, modes not trapped within the new crustal layer will leak out of the layer, rapidly at first, then at a steadily decreasing rate. This implies that wide angle reflections of energy escaping from the crustal layer towards the bottom boundary of the grid could possibly contaminate transition calculation results. However, the model grids do not extend far enough, in the x direction, beyond the transition for this to be a problem. The energy will encounter the rightmost end of the grid, either on the downgoing or the upgoing portion of its path, rather than reaching a receiver at or near the surface as a wide angle reflection. Since a wavefront which has a small angle of incidence with the bottom boundary has a large angle of incidence with respect to the end boundary, most of the amplitude of the wavefront incident on the right-most end boundary will be transmitted rather than reflected. Therefore, it is removed from the grid. Careful grid design will prevent significant contamination from wide angle bottom reflections.

CHANGES TO L_g WAVETRAINS ON PASSAGE THROUGH A C/O TRANSITION AND THEIR DEPENDENCE ON L

When a wavefield consisting of SH L_g mode sum energy passes through a C/O transition region such as that illustrated in Fig. 4(a) several important things happen. In order to clearly explain these effects and their variation with L one must think of the wavefield in terms of an incident wavefield, a reflected wavefield, and a transmitted wavefield. The transmitted wavefield is then subdivided into four subcomponents which will be useful in explaining the observed results. The entire wavefield, or any of its components or subcomponents can be interpreted as either a sum of modes or a sum or multiply reflected SH rays. To allow a clear definition of each of these components and subcomponents in terms of the ray interpretation the diagrams in Fig. 6 are critical.

Before each of the three components are defined the notation used in Fig. 6 must be explained. ϕ_{cm} is the angle between the base of the continental crust and the bottom boundary of the crustal layer in the transition region. ϕ_{oc} is the angle between the upper boundary of the crustal layer and the surface at $z = 0$. The incident angle and the angle of reflection for the nth interaction of a ray with a boundary (crust–mantle boundary, CMB, or crust–ocean boundary, COB) within the transition will be denoted j_n. Similarly, the transmission angle for the nth interaction of a ray with a boundary, will be denoted j'_n. As long as the ray remains in the transition region, $j_n = i - n(\phi_{c1} + \phi_{c2}) + \phi_{c2}$, where $\phi_{c1} = \phi_{oc}$ and $\phi_{c2} = \phi_{cm}$ if the first interaction is with the COB, and $\phi_{c1} = \phi_{cm}$ and $\phi_{c2} = \phi_{oc}$ if the first interaction is with the CMB. The angle of incidence is j_{oc} for rays transmitted into the oceanic crustal layer, and j_{con} for rays reflected back into the continental crustal layer. When the first reflection of the ray exiting the transition region, from the upper or lower boundary of either the continental or oceanic crustal layer, is the nth reflection then $j_{con} = j_{oc} = j_n + \phi_{oc}$, or $j_{con} \times j_{oc} = j_n + \phi_{cm}$, respectively.

The incident wavefield is composed of the trapped modal SH L_g energy arriving from the source, and is complete and untransformed only in the region of continental structure. If the incident wavefield within the continental structure is viewed as a superposition of multiply reflected post-critical SH rays with a range of incident angles, its components can be followed into the transition region. As the wavefield passes through the transition region the rays of which it is composed may each interact with the COB or the CMB. Each time a ray interacts with a boundary its incident angle j_n is reduced. A ray remains a component of the incident wavefield until an interaction with a boundary causes j_n to become negative and the ray to be turned back towards the source. Thus, the incident wavefield within the transition region is defined to be the superposition of all rays travelling towards the region of oceanic structure. A few sample rays of an incident wavefield are shown in Fig. 6(a). All rays within the crustal layer of the transition region, shown as solid lines, are part of the incident wavefield.

The reflected wavefield is composed of all the SH rays which have been turned back towards the source by their interaction with the CMB and the COB. Thus the reflected wavefield is a superposition of rays for which j_n has become <0 for some previous interaction with a boundary. An example of such rays can be seen in Fig. 6(a). The rays which are part of the reflected wavefield are shown as dotted lines within the crustal layer of the transition region. The reflected wavefield travels sourcewards through the crustal layer of the transition region, and the region of continental structure. In the region of continental structure the reflected wavefield can also be conceived of as a superposition of trapped and leading modes reflected from the transition region.

The transmitted wavefield is composed of all the energy transmitted through the transition region into the crustal layer of the region of oceanic structure, and all the energy transmitted into the mantle layer. The transmitted wavefield is divided into four components, two in the mantle layer, one in the crustal layer, and one in both layers in the region of oceanic structure. These components are all easily explained in terms of the SH ray interpretation. The two components within the mantle layer are the forward transmitted wavefield and the reverse transmitted wavefield. Only energy crossing the CMB into the mantle layer is included in these components. The forward transmitted wavefield is the portion of the incident wavefield which is transmitted across the CMB into the mantle layer when the rays forming the incident wavefield (rays with $j_n > 0$)

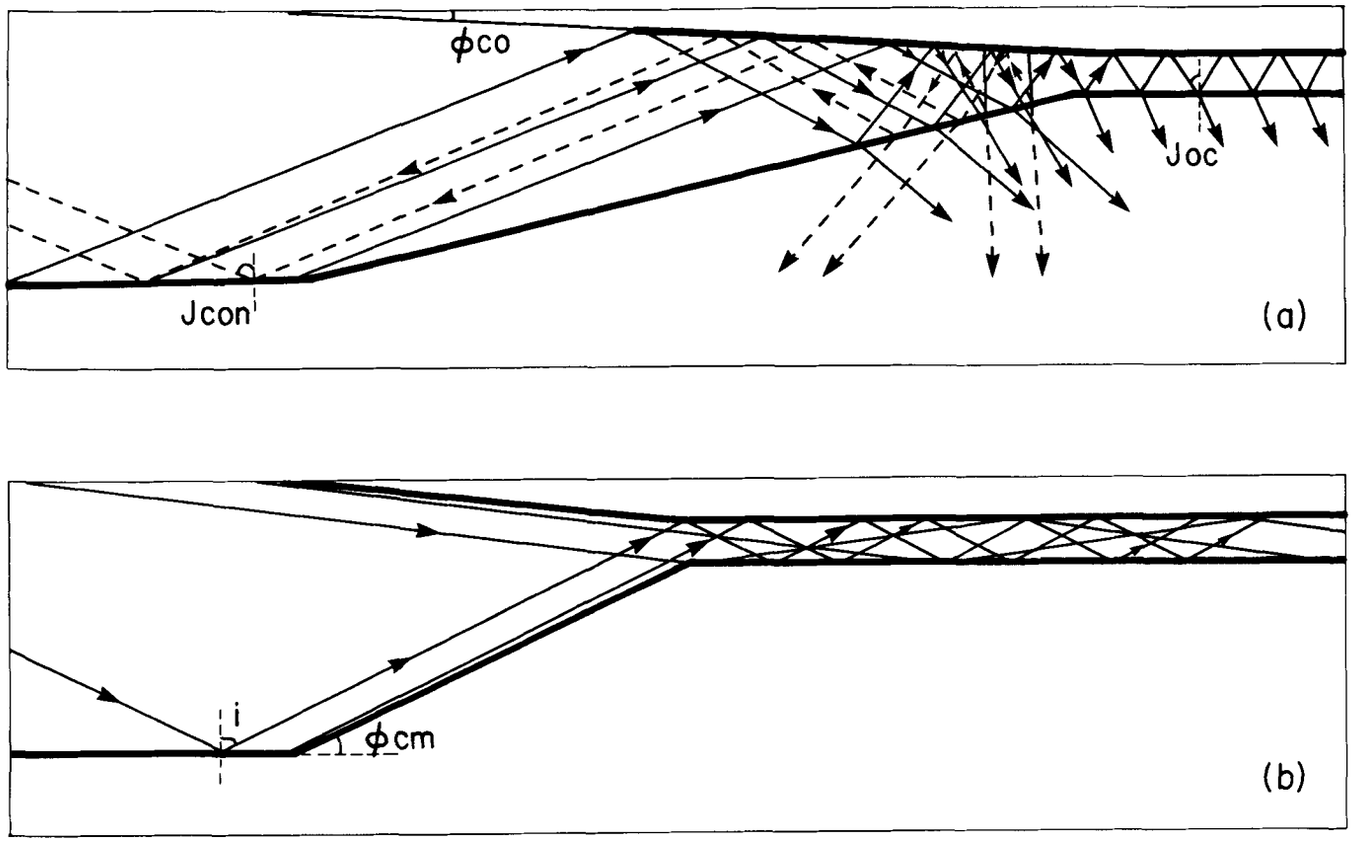

Figure 6. Definition of the components of the wavefield in terms of the ray interpretation. (a) shows examples of types of rays which constitute the incident wavefield (solid rays in the crustal layer), the reflected wavefield (dotted rays in the crustal layer), the forward transmitted wavefield (solid rays in the mantle layer), and the reverse transmitted wavefield (dotted rays in the mantle layer), within the transition region. (a) also shows an example of a type of ray which constitutes the transformed transmitted wavefield (solid ray transmitted through the transition into the crustal layer in the region of oceanic structure). Energy from the illustrated ray leaks into the mantle layer in the region of oceanic structure. Rays with post-critical angles of reflection in the crustal layer of the oceanic structure are produced similarly, and also constitute components of the transformed transmitted wavefield. (b) shows the types of rays which constitute the direct transmitted wavefield. All such rays travel through the transition region without interacting with the CMB or the COB.

interact with the CMB. All rays, shown as solid lines in the mantle layer of the transition region of Fig. 6(a), are components of a forward transmitted wavefield. The forward transmitted wavefield is present in the transition region and may propagate into the region of oceanic structure. The reverse transmitted wavefield is the portion of the reflected wavefield which crosses the CMB into the mantle layer when the rays which form the reflected wavefield (rays with $j_n < 0$) interact with the CMB. The reverse transmitted wavefield is present in the transition region and may propagate into the region of continental structure. Fig. 6(a) shows rays which form part of a reverse transmitted wavefield as dotted lines within the mantle layer of the transition region. The directly transmitted wavefield is a superposition of the SH rays in the incident wavefield that pass through the crustal layer of the transition region and into the crustal layer of the region of oceanic structure without interacting with the CMB or the COB. The rays are then trapped in the oceanic crustal layer. Some rays from a directly transmitted wavefield are illustrated in Fig. 6(b). The transformed transmitted wavefield is present only in the region of oceanic structure. It is composed of a superposition of rays which have interacted with the CMB and/or COB one or more times as they propagated through the transition region into the oceanic crust. These rays have values of $j_n > 0$ for their last interaction with the CMB and/or the COB in the transition region. The values of j_{oc} for these rays are appropriate for both pre-critical and post-critical reflections. Pre-critical reflections are equivalent to leaking modes. Energy from these modes is visible as amplitudes in the crustal layer and in the mantle layer. As the transformed transmitted wavefield propagates through the oceanic structure energy from these modes escapes the oceanic crust and propagates in the mantle layer. Post-critical reflections correspond to trapped modes and continue to propagate through the oceanic crustal layer.

All models used in this portion of this study have crustal SH velocity of $3.5\,\mathrm{km\,s^{-1}}$, crustal density of $2.7\,\mathrm{g\,cm^{-3}}$, mantle SH velocity of $4.5\,\mathrm{km\,s^{-1}}$ and mantle density of $3.5\,\mathrm{g\,cm^{-3}}$. All FE grids have the transmitting BC applied to all grid edges excepting the free surface and the surface on which the forcing functions are applied. All calculations use the same set of 60 forcing functions determined for a strike slip source at a depth of 8 km, a distance of 1500 km from the grid edge. Each of the components of the wavefield discussed above will be illustrated in the time slices or

seismograms for the 25 km C/O transition region. These time slices and seismograms are presented as an example of the general transmission properties of simple transition regions. The variation of such transmission properties with L will also be illustrated. The observed properties and their variations with L will then be explained.

A series of time slices for the 25 km C/O transition is shown in Fig. 7. In the first time slice the displacements entering the grid as dark, almost vertical bars are those which produce the largest peak to peak amplitudes in the seismograms. The second time slice shows the same high frequency arrivals after they have propagated about halfway through the transition region. The maximum amplitudes seen within the transition region of the third time slice are almost twice those seen in the unperturbed layer over a half-space wavefield seen in the first two time slices. So, the plotted amplitudes of all the displacements in the third time slice have been significantly reduced by scaling, making the same disturbances appear smaller. In the fourth time slice the highest amplitude regions of the wavefield have propagated past the right-most edge of the grid. The maximum amplitude is much smaller so the same disturbances appear to have much larger amplitudes. The fifth time slice shows a further amplification of the amplitude of the disturbances due to scaling. The amplification helps make the highest amplitude portion of the reflected wavefield (<5 per cent of incident amplitude) visible as a series of broken vertical bars near the left-most end of the grid. All sections of the incident wavefield show triangular regions of maximum amplitude. The extent of each triangular region, in the x direction, increases for regions of the wavefield incident on the left end of the grid at a later time. The end of the incident wavefield is seen, in the fifth time slice, about midway between the left grid edge and the arrow, to the right of the visible reflected component. The C/O transmitted wavefield is visible in the last three time slices as disturbances travelling through the half-space from the CMB towards the right-most edge of the grid. The reverse transmitted wavefield is clearly visible in the fifth time slice, and present in the last three time slices, as disturbances travelling through the half-space from the CMB towards the grid bottom and the source. For the earliest disturbances in the half-space the forward transmitted wavefield propagates along a path approximately parallel to the crust–mantle interface in the oceanic region, and the reverse transmitted wavefield propagates along paths nearly parallel to the CMB. As time progresses, the propagation paths of both the forward and reverse transmitted wavefields approach the normal to the CMB. Energy escaping from the through the oceanic crustal layer forms a forward bending arc of higher amplitudes in the mantle half-space. As the high amplitude regions of the forward transmitted wavefield propagate longer distances or propagate along paths with larger vertical components, the tails forming due to leakage from the oceanic crustal layer detach from the forward transmitted wavefield.

Figure 8 shows seismograms recorded at the receivers along a surface section. These seismograms illustrate the magnitude of the concentration of amplitude at the surface of the crust seen in the time slices, and the change in the waveforms as the wavefield passes through the transition. Fig. 9(a) shows the variation of 60 s rms amplitude with distance, $X2$, from the source for each of the C/O transition FE calculations. Amplitudes produced using the different C/O transition lengths are plotted at the same scale and are proportional to the source strength. The numerical values of amplitude shown on the amplitude axis are chosen so that the maximum value on the axis is one. To avoid blank spaces in the plots the minimum value was not chosen to be zero. The amplitudes recorded at nodes along the surface of the crustal layer within each transition region show a general increase as one moves from B towards D. The duration of the coda with amplitudes above one-third of the maximum peak to peak amplitude is also increasing. This increase in coda length supports the attribution of the later portions of the observed coda to diffraction and reflection from crustal structure. The size of the increase in rms amplitude is smallest for the step transition and increases as L increases. Superimposed on the general increase is an oscillatory term. The method of scaling the distance coordinate within the transition region, in Fig. 9, makes the coincidence of maxima and minima at approximately the same fraction of the transition length for all L's considered very clear. Increases in amplitude before reaching distance B are due to energy reflected from the transition boundaries back towards the source. The amplitude increase near B is largest for a step transition and decreases as L increases. The fluctuations in amplitude following the transition region show that the wavefield has not completely adjusted to the oceanic structure in the few kilometres beyond the transition regions illustrated in this figure.

Figure 10 shows seismograms recorded on depth sections at distances B and D. Fig. 11 shows the variation of 55 s rms amplitude with depth at several distances. The seismograms shown in Fig. 10(b) are recorded at the depth of the surface of the oceanic crustal layer. They show a 50 per cent increase in amplitude as the energy travels from B to D. They also show that the amplitude of the coda becomes a larger portion of the maximum peak to peak amplitude, that is the envelope of the coda decays more slowly at D than at B. An increase in rms amplitude (20 per cent) and a slower coda decay is also seen if the free surface seismograms at B (Fig. 10a) and D (Fig. 10b) are compared. The seismograms recorded at the nodes at the depth of the bottom of the oceanic crustal layer (Fig. 10c) show a small decrease in rms amplitude across the transition. Comparing Fig. 11(b) and (d) the increase at the surface of the oceanic crust and the decrease at the base of the oceanic crust are clear for all transition lengths. Examination of seismograms at the nodes at distances B and D with depths between Fig. 10(b) and (c) shows that the amplitude increase between B and D is largest at the surface of the crust and decreases rapidly towards the base of the crust. This statement is supported by the amplitudes illustrated within the crust in Figs 11(b) and (d). These amplitudes in Fig. 11 form a summary subset of many measurements. Comparison of the seismograms at B and D in Figs 10(d) and (e) show that the amplitudes of the seismograms at depths below the base of the oceanic crust are decreased by passage through the transition region, from B to D. The transmitted waveforms are similar to the incident waveforms. The reduction in transmitted amplitude increases as depth increases. The latter observation is more obvious when the amplitude versus depth plots in Figs 11(b) and (d) are compared. Figs 11(a) and (b) shows that small

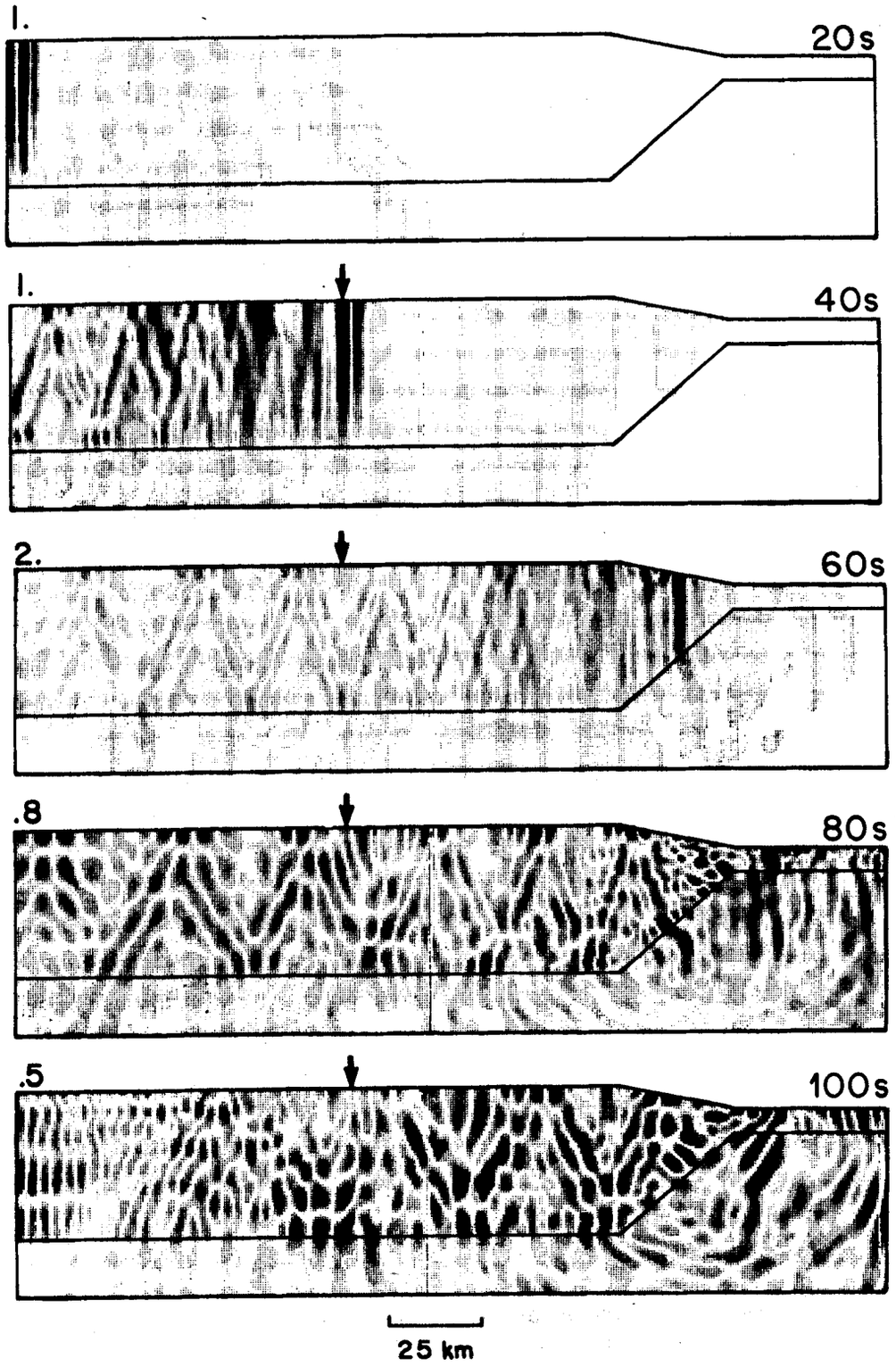

Figure 7. Time slices recorded during the 25 km C/O transition calculation. The crustal layer and the ends and bottom of the FE grid which contain it are outlined. Displacements are graphically represented by symbols plotted at an array of points depicting the nodes in the FE grid. The size of the symbol plotted at the node is increased as the absolute value of the displacement increases, producing darker areas where larger displacements are occurring. Each of the time slices is self scaled, that is the largest value of the absolute value of amplitude in the grid is set to the largest symbol size. A minimum amplitude cut-off of 2 per cent is defined below which no symbol is plotted. Sixty forcing functions were used. The time since the initiation of the FE calculation is shown above the right end of each grid. The arrow above a time slice shows the location to which the disturbances moving at 3.5 km s^{-1}, seen at the left end of the previous time slice, have moved in the intervening duration. The number above and to the left of each time slice is the scaling factor to bring that time slice to the same amplitude as the first time slice.

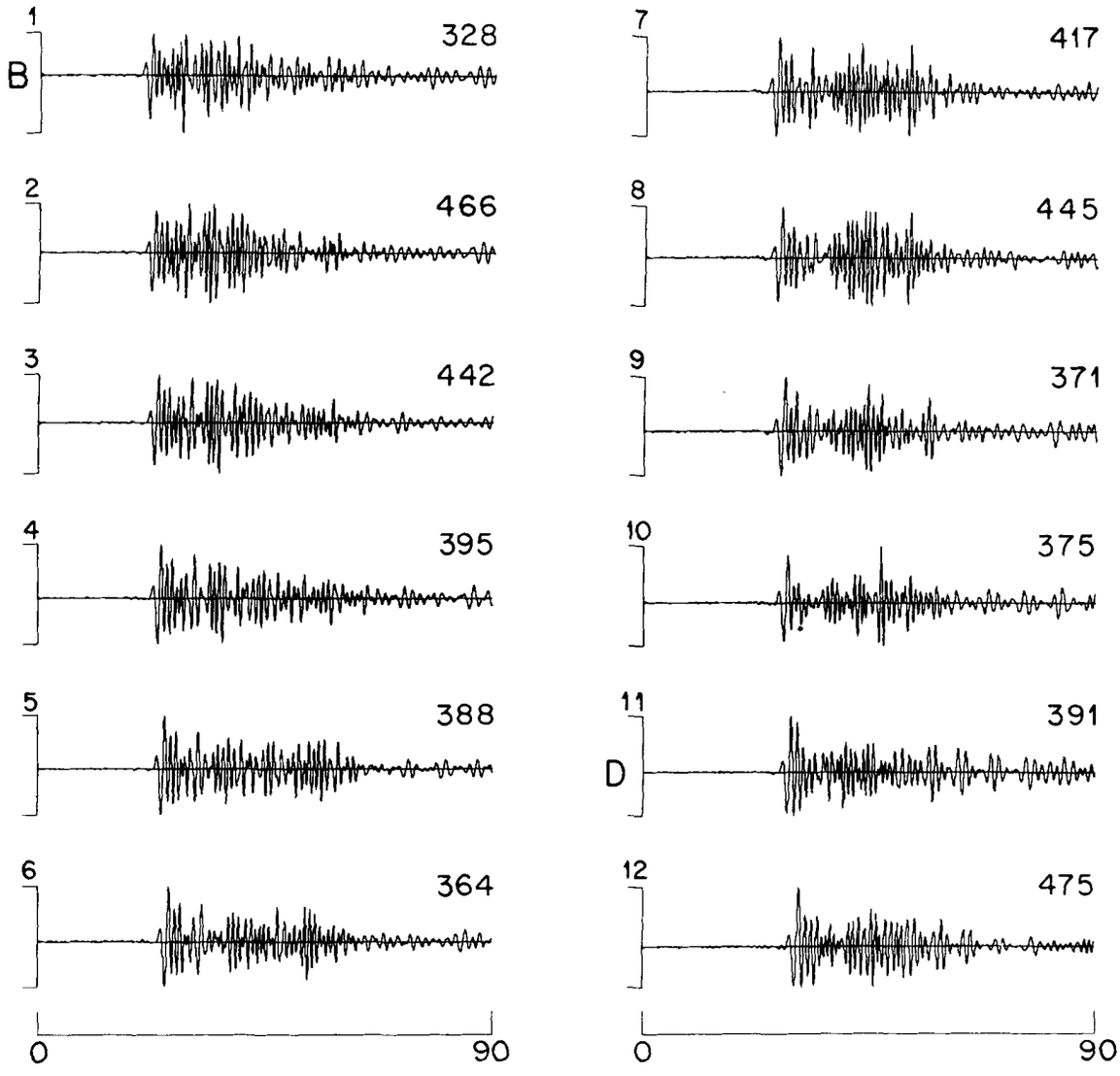

Figure 8. Surface section of seismograms recorded for a 25 km C/O transition calculation. The numbers to the left of each seismogram indicate the location of the node at which that seismogram is recorded. Seismogram 1 was recorded at B, seismogram 11 at D. The numbers increase as one moves farther from the source. The spacing between receivers in the transition zone is uniform. The numbers above the right end of each seismogram give the 60 s, rms amplitude of that seismogram.

amplitudes are seen at depths below the continental crustal layer. A large discontinuity in amplitude occurs at the base of the continental crust. Fig. 11(c) shows that this discontinuity remains at the depth of the base of the crustal layer within the transition region. Fig. 11(c) also shows that the amplitudes in the mantle layer within the transition region are maximum immediately below the CMB, and decay rapidly with depth below that boundary. Fig. 11(d) shows that the amplitude of the transmitted seismograms, in the mantle layer above the depth of the base of the continental crust, at D, decreases as L increases. Below the depth of the base of the continental crust amplitudes at D increase as L increases. At distances E and F (Figs 11e and f), further from the transition region, the magnitudes of these trends decrease. These observations are further support for the observation that as L increases larger energies are transmitted across the CMB and that these energies propagate downwards more rapidly.

The triangular pattern of maximum amplitudes in the wavefields (Fig. 7) can easily be explained. Consider the SH L_g energy in the crustal layer as a superposition of post-critically reflected multiple SH wave reflections. The critical angle is about 51°. Since the wavefront is perpendicular to the ray, the wavefronts that are visible as the triangular regions of maximum amplitudes should show angles of incidence with the bottom boundary of the crustal layer of between 0° and 39°. These are indeed the incident angles the wavefronts in the time slices (Fig. 7) are observed to exhibit. Near the front of the wavefield the dominant angles of incidence are near 0°, that is the regions of maximum amplitude are almost vertical. Later in the wavefield the dominant angles of incidence increase causing the widening triangular patterns of maximum amplitude. The increase in width of the triangular regions corresponds to a decrease in group velocity which can be translated to a decrease in period and/or a larger contribution from higher

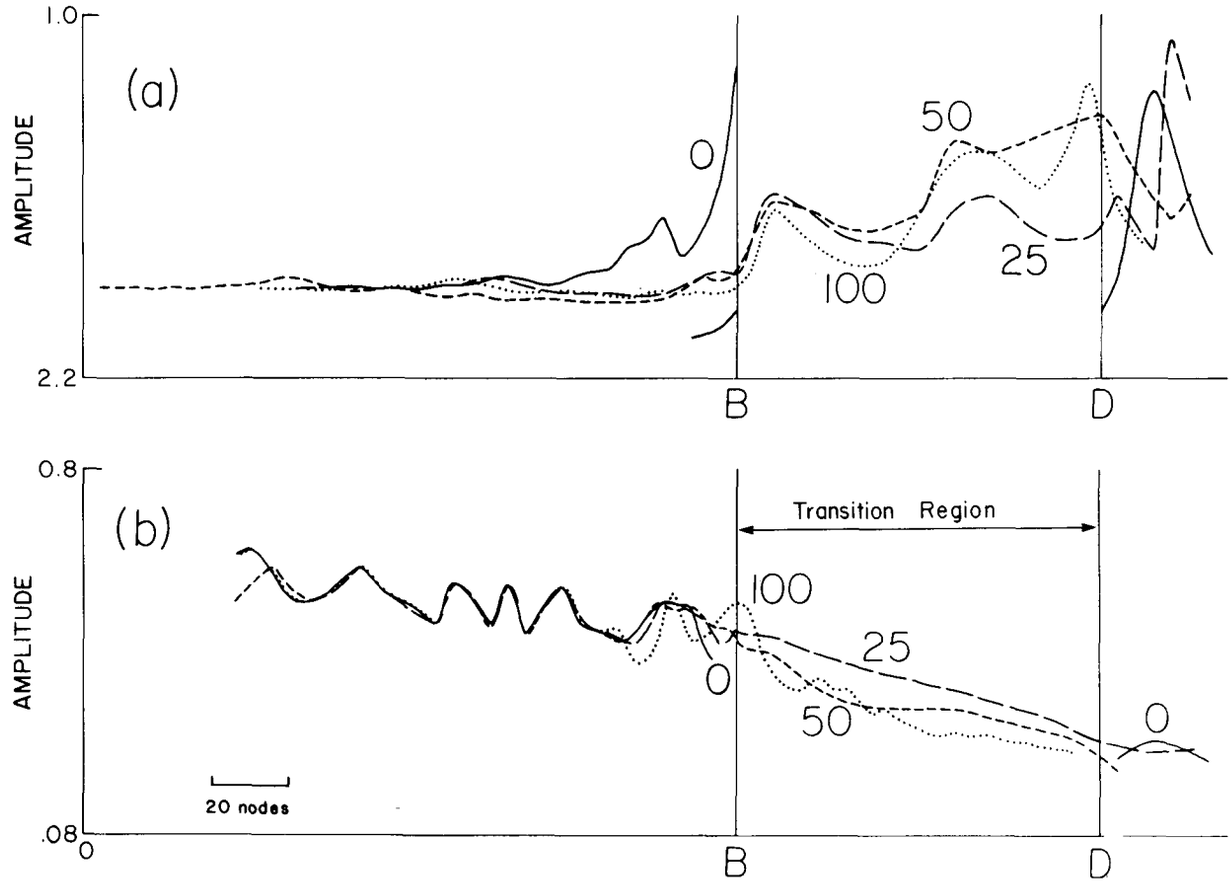

Figure 9. Variation in rms surface amplitude with distance, $X2$, from the source for (a) each C/O transition calculation (60 s rms), and for (b) each O/C transition calculation (50 s rms); rms amplitude is the y coordinate. The two vertical lines labelled B and D, indicate the limits of the transition region. Outside the transition region the scale is uniform. The distance scale (x coordinate) in the transition region is different for each L. Within the transition region all distances are plotted with respect to an origin at B, as fractions of L. Each line, labelled with the L it represents, was generated using rms measurements at intervals of 5 km along the crustal surface.

modes. The later parts of the seismogram are predominantly higher mode energy.

The growth in amplitude for seismograms at crustal surface nodes as distances range from B to D can be explained in terms of energy concentrated in the thinning crustal layer of the transition region. As j_n decreases toward zero for successive n's, the reflection points at the boundaries in a transition region are separated by smaller horizontal distances (Fig. 6a). This implies that the density of rays will increase as the crustal layer thins, thereby producing higher amplitudes. An equal concentration would be expected at the CMB if no energy was transmitted across that boundary. In fact, for a model with the same geometry but with the mantle half-space replaced by water to disallow transmission across the CMB, an amplification of 75 per cent is observed at both boundaries. However for continent ocean boundary models, as j_n and thus, j'_n, decrease the displacement transmission coefficient,

$$T_n(j_n) = \frac{2\cos(j_n)}{\cos(j_n) + 1.62\cos(j'_n)},$$

increases. When more energy is concentrated at the CMB more energy is transmitted across it. The escape of energy from the crustal layer to form the transmitted wavefield also explains the distribution of amplitude with depth within the crustal layer of the transition. The amount of concentration of amplitude increases as the distance from the CMB increases and the effects of the energy escaping across it become weaker.

Extending the above arguments explains the increase in the amount of concentrated energy, the increase in the magnitude of the transmitted wavefield, and the decrease in the amplitude of the reflected wavefield as L increases. Figs 12(a) and (b) show a pair of ray diagrams for a 25 km C/O transition region, Figs 12(c) and (d) shows a similar pair of ray diagrams for a 100 km C/O transition. These diagrams are useful when explaining the trends observed in the results presented above, and their dependence on L. Comparing Figs 12(a) and (c) or (b) and (d) shows that as L increases the angles ϕ_{cm}, and ϕ_{co} decrease causing j_n to decrease more slowly and allowing the number of reflections, m, within a transition to increase. When L increases, the increase in m causes an increase in ray density and explains the increase in concentrated amplitude at the COB. When L increases, by the same arguments, the amount of energy concentrated at the CMB also increases. The transmission of this energy across the CMB causes the amplitude of the transmitted wavefield to increase as L increases. It should be noted that increasing L reduces the rate at which the

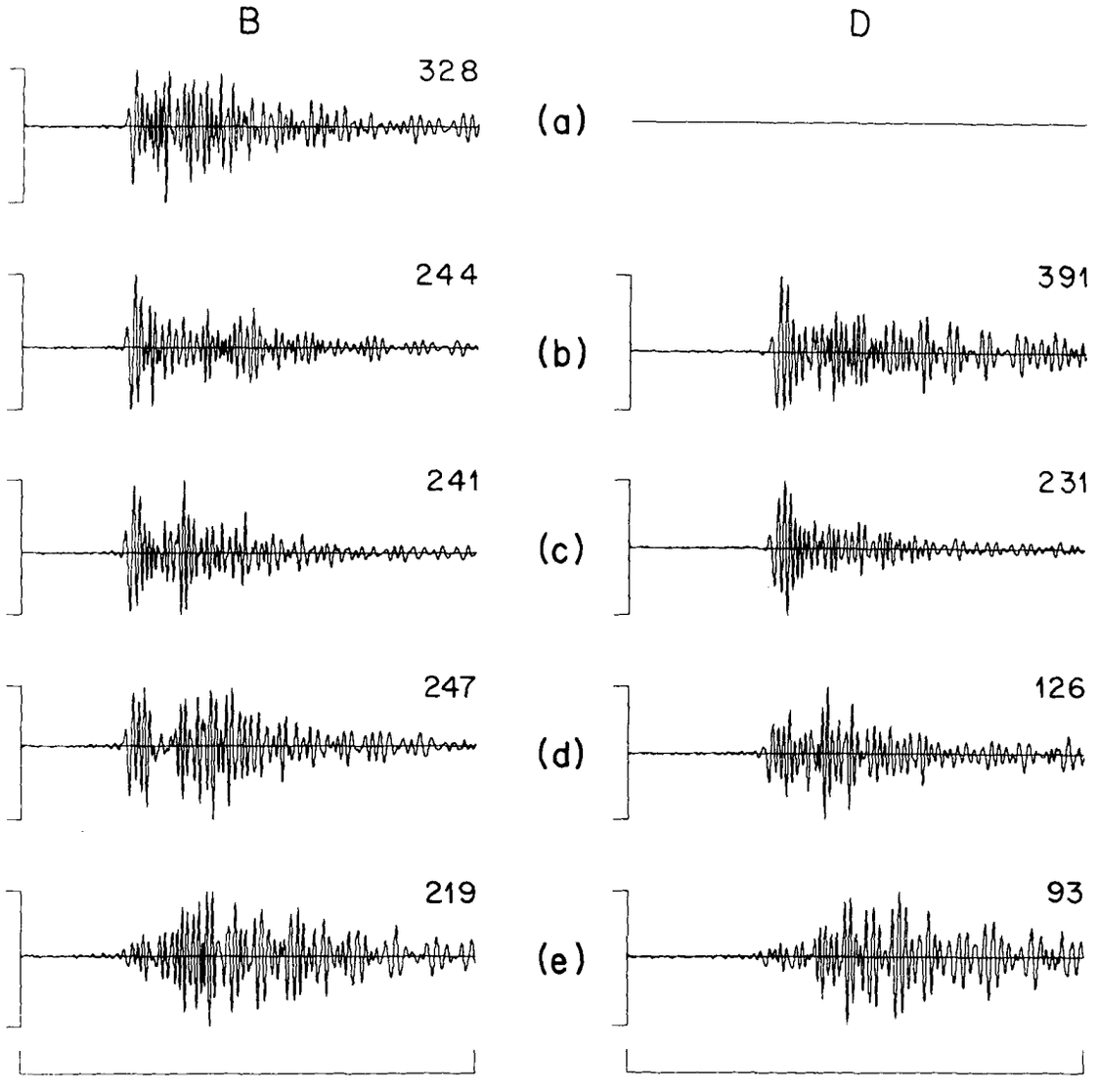

Figure 10. Depth sections of seismograms recorded at B and D for a 25 km C/O transition calculation. The numbers above the right end of each seismogram show the 60 s rms amplitude. Successive rows show pairs of receivers at increasing depths. (a) shows receivers at the depth of the surface of the continental crust, (b) shows receivers at the depth of the surface of the oceanic crust, (c) shows receivers at the depth of the base of the oceanic crust, (d) shows receivers midway between (c) and (e), (e) shows receivers at the depth of the base of the continental crust.

crustal thickness changes, so at a given distance from the beginning of a transition region the change in amplitude transmitted across the CMB per unit horizontal distance becomes smaller as L increases. However, integrated over the entire length of the transition region the amount of energy transmitted across the CMB increases. Since the amount of amplitude concentrated at the COB and thus transmitted into the oceanic crustal layer, and the amount of energy concentrated at the CMB and thus transmitted across the CMB both increase as L increases the amplitude of the reflected wavefield must decrease as L increases. Let seismogram A be a hybrid seismogram recorded on depth section A (Fig. 4) in a C/O transition calculation. Let seismogram B be the hybrid seismogram, recorded during the continental reference calculation, at the same depth and distance from the source as seismogram A. The reflected component is measured by analysing the component which remains when seismogram B is subtracted from seismogram A. Reflected amplitudes measured in this manner show a clear decrease as L increases.

Figure 12 can be used to explain how and why the direction of propagation of the forward and reverse transmitted wavefields varies as time progresses. When the arrivals of the highest group velocity reach the CMB the resulting forward transmitted wavefield travels along a path approximately parallel to the crust half-space interface in the oceanic structure, and the resulting reverse transmitted wavefield travels along a path almost parallel to CMB. The incident angles j_n are maximum. As $|j_n|$ for a given n, and the group velocity, decrease the values of j'_n decrease. Thus, the propagation direction of both transmitted wavefields approach the normal to the CMB. As L increases larger values of n are possible within the transition region. For each value of n a transmitted wavefield is created at the CMB. Therefore, the range of propagation directions seen at a given time increases as L increases.

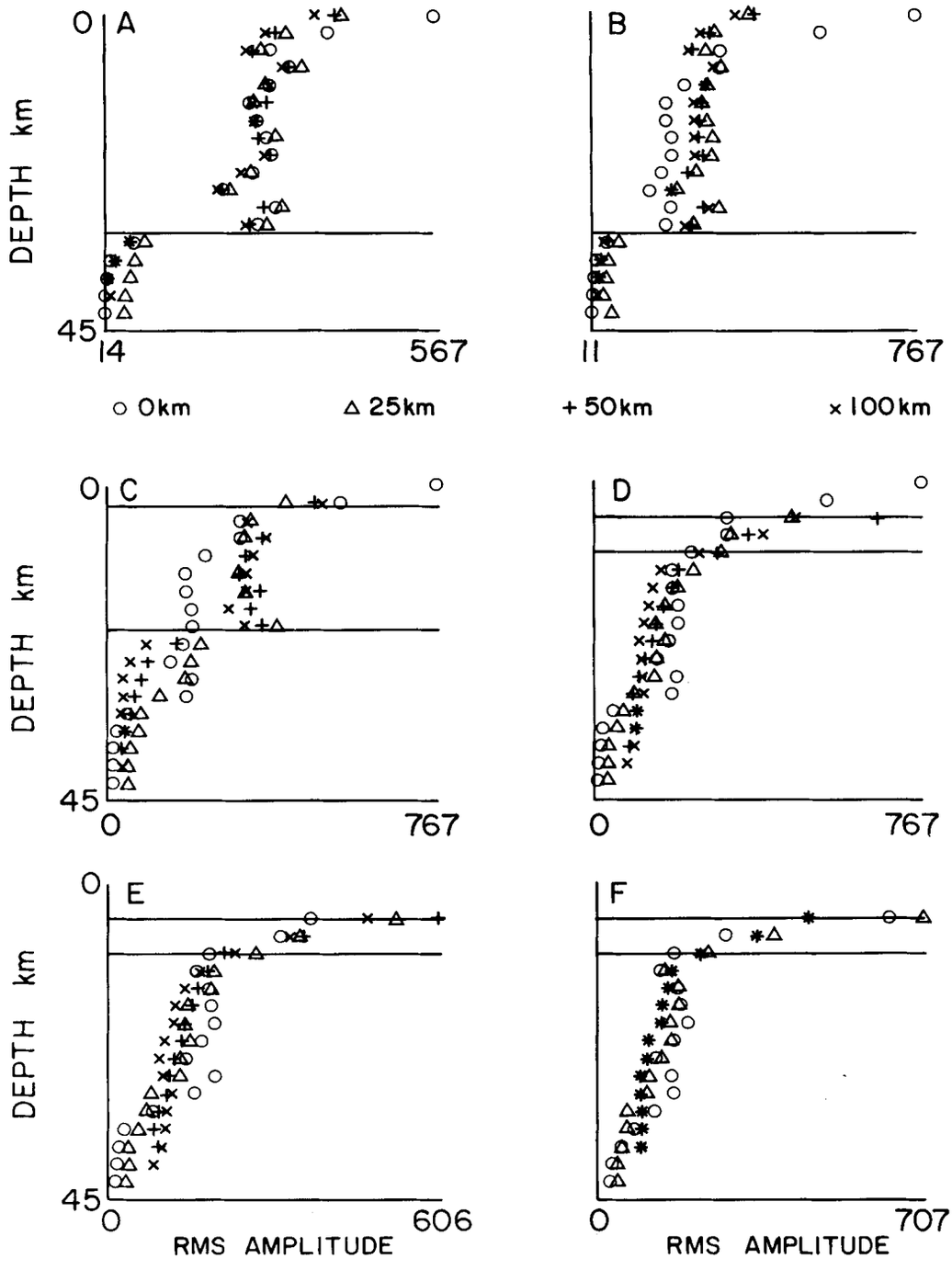

Figure 11. Variation of 55 s rms amplitude with depth on depth sections A, B, C, D, E, of Fig. 4, and F, located 10 km beyond E, for each C/O transition model. Each plot illustrates results for one depth section. The letter at the upper left of each plot identifies the location of the depth section. Amplitudes for the surface node and nodes equally spaced down the depth section ($\Delta z = 2.5$ km) are shown. The two solid horizontal lines on each diagram show the base and top of the crustal layer at the location of the depth section. If only one solid line is present then it indicates the base of the crust. In this case the surface of the crust is at the top of the vertical axis.

The magnitude variations of the directly transmitted wavefield and the transformed transmitted wavefield can also be easily explained. Let the thickness of the oceanic crust be T_{croc}, and the thickness of the continental crust be T_{crcon}. For reflections immediately preceding the beginning of the transition region some rays ($i > 90 - \arctan[(T_{crcon} - T_{croc})/L]$) can propagate through the transition region without interacting with either the CMB or the COB. These rays, which form the directly transmitted wavefield, continue to bounce with the same post-critical angles of incidence at the crust–mantle interface and the free surface as they did in the continental structure. They represent the energy transmitted through the transition directly, without changes in period or phase velocity. For these rays no mode conversion has occurred and no energy has been converted to other phases. These rays form the unchanged components

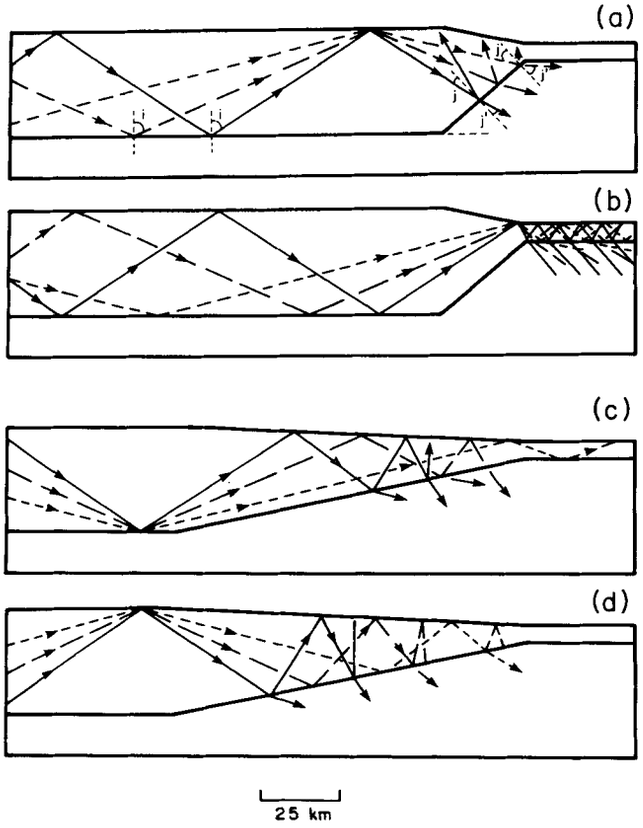

Figure 12. Illustration of ray paths within a 25 and a 100 km C/O transition structure. Diagrams are drawn to scale. Each diagram shows rays with angles of incidence, i, 55°, 65°, and 75°, at the free surface and crust–mantle interface in the continental portion of the model. These angles sample the possible range of post-critical incident angles (>51°). The incident angle, j_n, and the transmission angle, j'_n, at the crustal boundaries in the transition regions are labelled. The upper diagram in each pair shows propagation paths for rays that encounter the CMB before the COB. The lower diagram shows propagation paths for rays that encounter the COB before the CMB. The arrows indicate the direction of propagation of the wavefront along the ray.

of the eigenfunctions defining each mode. The range of angles, i, over which the direct transmission ocurs decreases as L increases. Thus, more unconverted energy is transmitted through shorter transitions. In contrast, the transformed transmitted wavefield is composed of rays which interact with the CMB or COB before being transmitted into the oceanic crustal layer. Such rays show changes in group velocity that indicate modal conversions are occurring. Energy is also converted into other phases as it escapes across the CMB to become part of the forward transmitted wavefield. As discussed above, the energies transmitted into the oceanic crustal layer and across the CMB both increase as L increases. As L increases, this increased transmitted energy is partially counteracted by the effects of decreased transmission of unconverted energy. This helps explain why the differences due to L are small.

The diagrams in Fig. 12 demonstrate why energy crosses the crust–mantle interface in the oceanic structure following the transition, why this transmitted energy is maximum near the transition and decreases as the distance from the transition increases, and why this transmitted energy increases as L decreases. The paths illustrated in the second 25 km transition outline show one-way modes which are not of appropriate frequencies to be trapped within the oceanic crustal layer, enter that layer. Analogous paths for rays which interact first with the CMB or rays which interact multiple times with the crustal boundaries in the transition region also exist. All such rays produce rays at pre-critical, $j_{oc} < 51°$, angles within the oceanic crust. For any such ray, the transmission coefficient at each successive reflection from the crust–mantle interface is $T(j_{oc})$. Thus, the proportion of reflected amplitude remaining in the crust after the nth bounce is $A_n = [1 - T(j_{oc})]^n A$, where A is the original amplitude. Clearly, the amount of escaping energy decreases with distance. For a shorter transition j_n, for a given i, is smaller. Thus, a larger range of angles $j_{oc} < 51°$ are produced for each path through the shorter transition. This means a higher density of pre-critical rays and higher amplitudes in and escaping from the oceanic crustal layer of shorter transitions.

The use of the interpretation of L_g waves in terms of multiply reflected SH rays to explain the FE results has been instructive. However, the many interacting effects involved in determining the properties of the reflected, converted, and transmitted wavefields would be extremely difficult to predict using this approach. Thus, the FE method is necessary to determine which effects are important and which need not be considered.

CHANGES TO L_g WAVETRAINS PASSING THROUGH AN O/C TRANSITION REGION: THEIR DEPENDENCE ON L

Next we will consider the passage of a wavefield consisting of SH type L_g mode sum energy, which has already passed through a continental region followed by a C/O transition region of 50 km length, through an O/C transition. An example of an O/C transition is illustrated in Fig. 4(b). Propagation through such an O/C transition has several effects on the wavefield. Results of the calculations for propagation through a 50 km O/C transition will be presented in detail so as to illustrate these effects. The O/C transition tests using a variety of L's will be summarized to illustrate how these effects depend on L. The noted effects and their variations with L will be explained. The set of forcing functions used to drive the O/C FE calculations were recorded during the FE calculation for the 50 km C/O model.

Before proceeding to these discussions the errors introduced due to the truncation inherent in coupling the C/O transition FE results into the O/C transition grid should be mentioned. The finite vertical extent of nodes driven by forcing functions at the left-most edge of the O/C transition grid will cause a vertical truncation of the incoming wavefield. Also, any reflections included in the seismograms recorded for use as forcing functions will be added to the forward propagating wavefield in the O/C calculation. These effects tend to increase the amplitudes at the surface of the oceanic layer near the left end of the grid. The uncertainties introduced by the coupling process appear to increase the amplitudes in the second grid by as much as 3 per cent. Therefore, they could possibly lead to a slight

underestimate of the magnitude of the attenuation effect, but should not lead to an overestimate.

A series of time slices, shown in Fig. 13, illustrates the FE calculation results for the 50 km long O/C transition. The highest amplitude concentrations visible in the first four slices correspond to the maximum amplitudes in the seismograms illustrated in Fig. 14. The first two time slices illustrate the wavefield travelling through the oceanic structure. The third time slice illustrates the passage of the highest amplitude portions of the wavefield through the transition region. In the fourth time slice these highest amplitude regions appear at the right-most end of the grid. In the fifth time slice they have exited the grid. The maximum amplitude in a given time slice decreases with time in the third to fifth time slice. The maximum amplitudes in the transition region decrease as the wavefront proceeds through the transition region. Thus, normalizing by the largest amplitude in each slice causes identical disturbances to increase in extent and intensity in successive slices. Triangular regions of maxima can be seen in the oceanic crust but they are not nearly so clear as those seen in the continental crust of the C/O transition. The third and fourth time slices clearly show that the energy which was previously trapped in the oceanic crustal layer

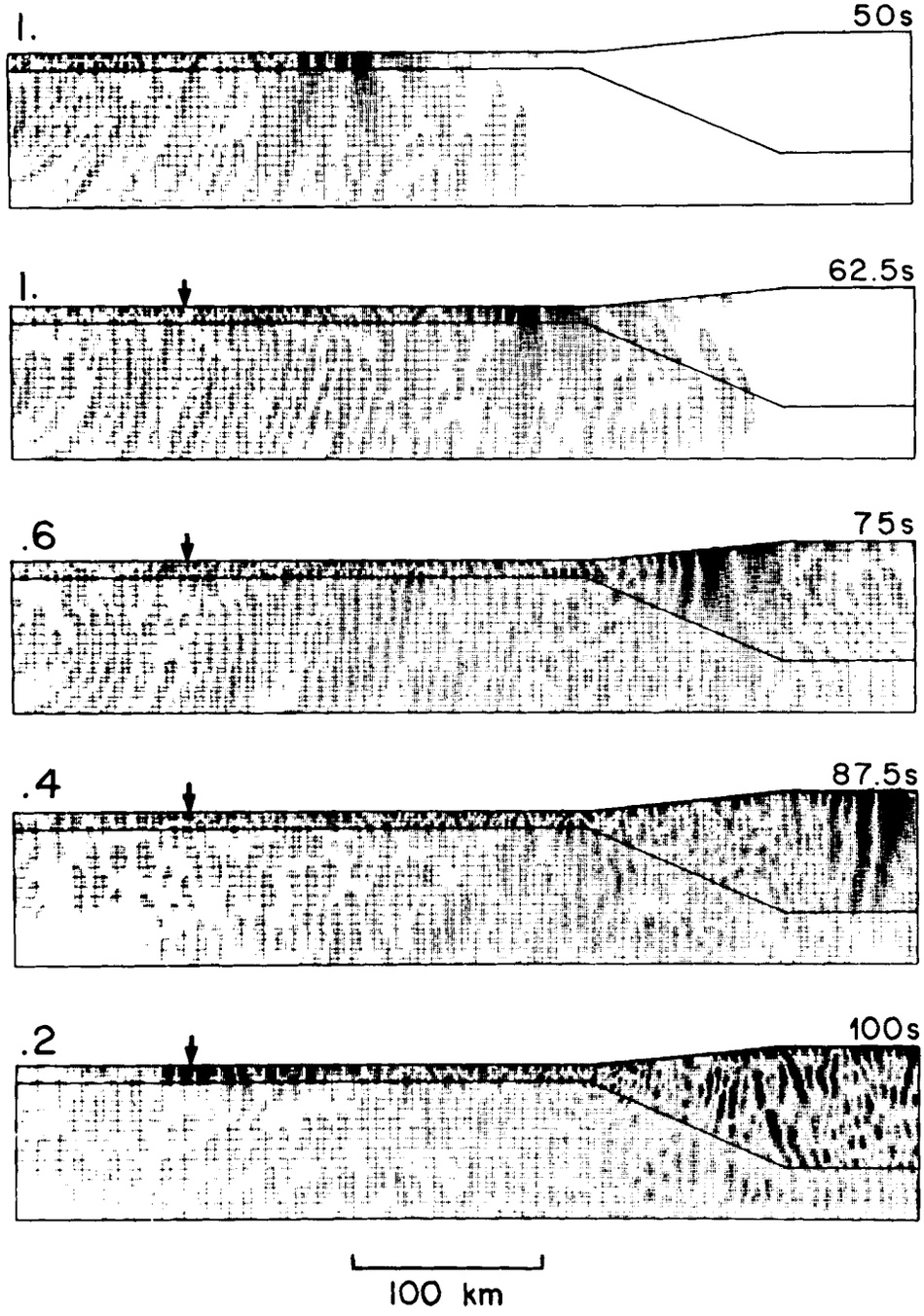

Figure 13. Time slices recorded during the 50 km O/C transition calculation. Details are identical to Fig. 7. 40 s rms amplitudes are shown.

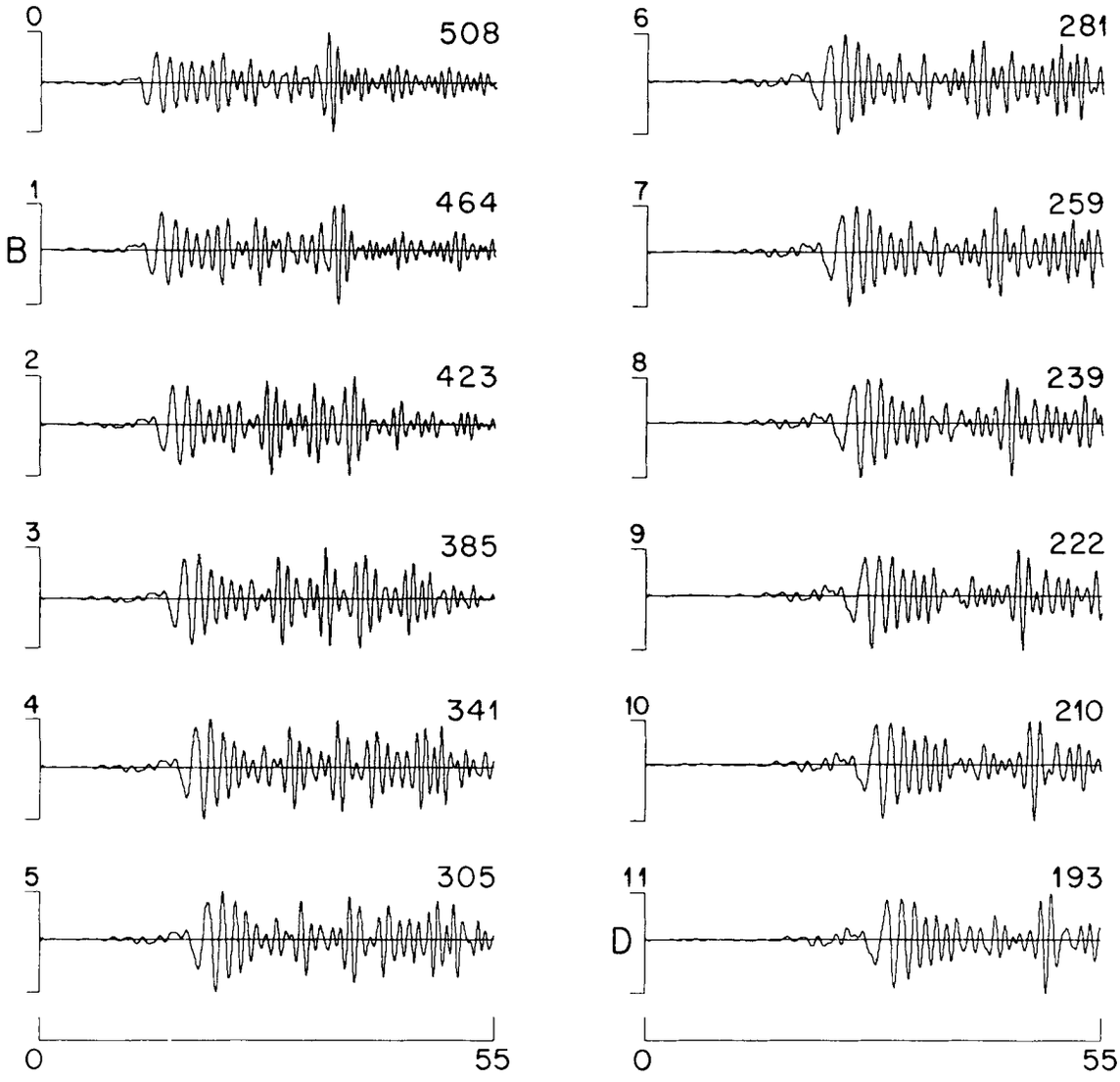

Figure 14. Surface section of seismograms recorded for a 50 km O/C transition calculation. Details explained in Fig. 8.

distributes itself throughout the crustal layer as it passes through the transition region and the region of continental structure. The amplitudes remain much larger near the surface, and decay rapidly with depth. The fifth time slice shows triangular regions maximum amplitude are beginning to appear in the continental structure. Further propagation in x is necessary before the wavefield becomes fully adjusted to the new layering in the region of continental structure.

The disturbances seen in the half-space of the oceanic region of the O/C transition grid contain significant energy. Examining the time slices shows that for a subset of these disturbances, equivalent to the forward transmitted wavefield discussed earlier, the z component of translation in the half-space is increasing for successive groups of disturbances. This is due to the interactions at the CMB in the C/O transition as explained earlier. It is more visible in these time slices than the C/O transition time slices due to the increased distance from the CMB. It is clear that these packets of amplitude are translated rapidly enough in z that some will pass into the half-space below the continental crustal layer before they reach the O/C transition region. Thus, the energy contained within them escapes the system and is not reconverted to L_g energy when the wavefield passes through the O/C transition. The amount of energy escaping from the system in this manner increases as L, or the length of the intermediate oceanic path, increases.

Figure 14 shows a surface section of seismograms for a 50 km O/C transition. Fig. 9(b) shows the variation of 55 s rms amplitude with distance, $X2$, from the source for each of the O/C transition FE calculations. A decrease in rms amplitudes is seen as one moves along the surface of the oceanic crustal layer approaching the transition region. This decrease is clear for short rms windows and almost vanishes for window length of 65 s or more. This indicates that the portion of the coda with amplitudes comparable to the maximum amplitude is decreasing in length, that is, that the rate of coda decay is increasing. Superimposed on this slow decrease in amplitude is an oscillatory term with amplitude approximately 15 per cent of the mean amplitude at the surface in the oceanic structure. The rms amplitudes

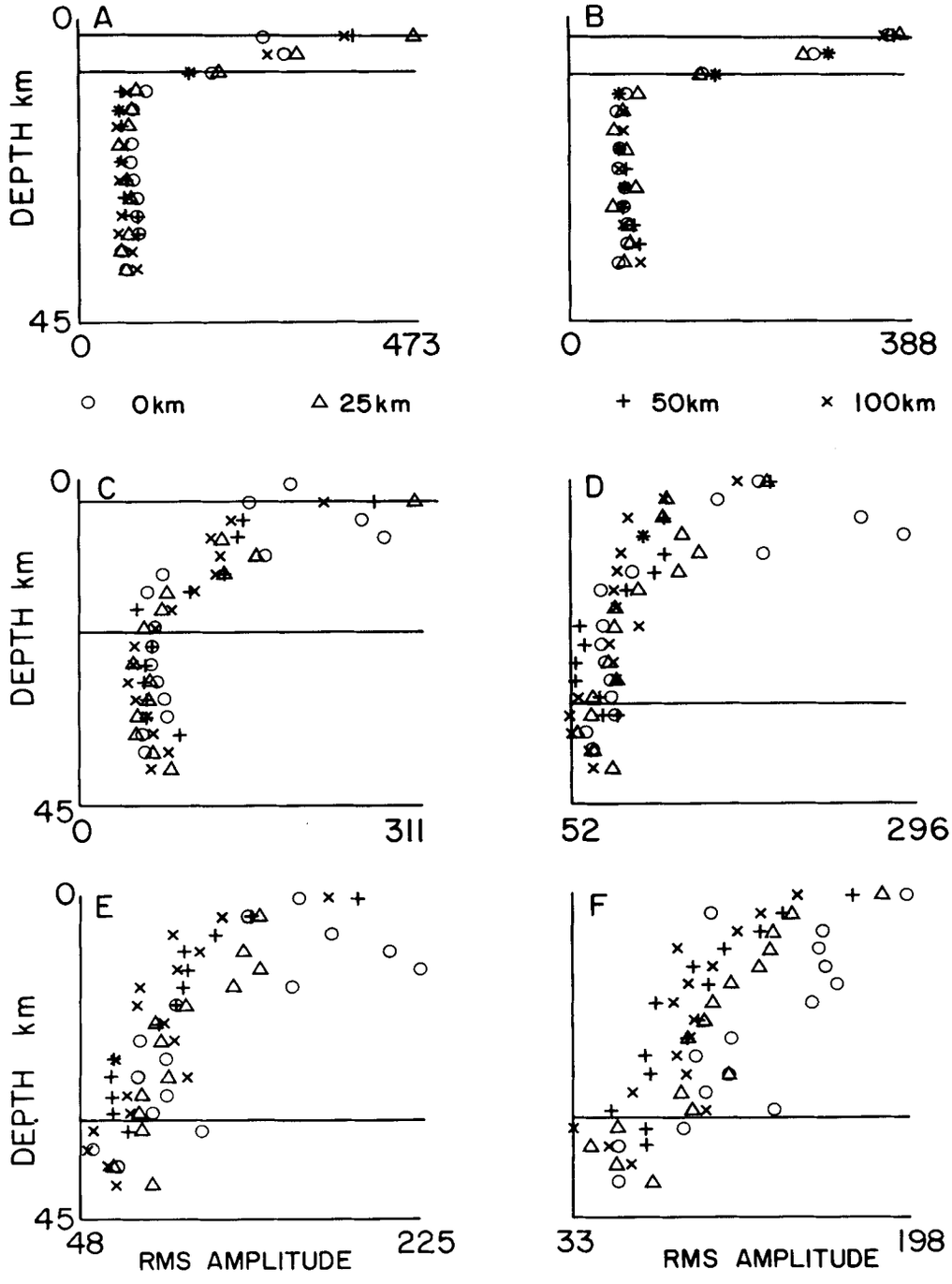

Figure 15. Variation of 55 s rms amplitude with depth. Details are as explained in Fig. 11.

recorded at nodes along the surface of the crustal layer within each O/C transition region decrease as one moves from B towards D. The size of this decrease is smallest for the step transition and increases as L increases. The rate of decay shows some tendency to become smaller towards the end of the transition. The superimposed oscillations seen in the O/C transition results are much smaller than those seen in the C/O transition results. They appear to be confined near the beginning of the transition region. The oscillation in amplitude following the transition region shows that the wavefield has not fully adjusted to the continental structure in the few kilometres beyond the transition regions illustrated in Fig. 9(b). Additional results which are not illustrated show the rms amplitude continues to decrease slowly until the wavefield readjusts to the new continental structure.

Figure 15 shows the variation of 55 s rms amplitude with depth. At the depth of the surface of the oceanic crustal layer propagation through the transition reduces the rms amplitude by more than a factor of two, and the peak to peak amplitude by 25 per cent. This indicates that the duration and amplitude of the coda are decreasing more rapidly than the amplitude of the largest arrival. At depths between the surface of the continental crust and the surface

of the oceanic crust amplitude decreases with depth. Then energy incident on the MCB is largely transmitted across the MCB into the crustal layer. Some of this energy eventually escapes across the CMB in the region of continental structure. The amplitudes below the crustal layer of the transition region decrease slowly with depth or even increase with depth. An increase of amplitude with depth below the crustal layer indicates that energy is travelling down towards the grid bottom and out of the system being considered.

Most of the energy incident on the MCB is transmitted across it. Thus, in the last four time slices, the reflections from the MCB are not easily distinguished from the later portions of the incident wavefield. The pattern of displacements seen in the oceanic half-space is distorted when the energy producing it is transmitted across the MCB. The uppermost portion of a disturbance crosses the boundary first and begins to move more slowly. The remainder of the disturbance, still in the mantle layer continues to move with the mantle's faster velocity. As the disturbance moves through the length of the transition, an increasing proportion of it moves into the crustal layer. This results in a slope being superimposed on the portion of the disturbance which has propagated back into the crustal layer. The slope,

$$\text{Slope} = \frac{L(v_M - v_c)}{v_M},$$

is dependent on L, the velocity in the crustal layer, v_c, and the velocity in the mantle, v_M. The slope, in this case about tan 52°, is observed easily in both the second and third time slices. It is also seen in the fourth and fifth time slices. However, in these time slices the amplitude incident from the oceanic crustal layer dominates that transmitted from the oceanic mantle layer making observation of the slope more difficult. If a realistic Q model were included the energy travelling through the half-space would be attenuated faster than the energy travelling through the crustal layer. However, since the energy incident from the oceanic crustal layer dominates in the highest amplitude portions of the trace, the increased attenuation in the half-space should not be important in this study.

The effect of the O/C transition region on the energy previously travelling in the oceanic crustal layer will now be discussed. Concentrations of amplitude incident from the oceanic crustal layer travel up the surface of the OCB. As they propagate up the OCB the lower edge of the amplitude concentrations are no longer constrained by the lower edge of the oceanic crustal layer. Consequently the energy can migrate downwards towards the depth of the base of the continental crustal layer. This diffusion of energy can be explained using a mechanism which is the converse of that used to explain the concentration of energy in the C/O transition. The incident angle for the ray perpendicular to each wavefront, j_n, increases as n increases. Subsequent reflection points are separated by larger horizontal distances producing a dilution in ray density and thus a decrease in amplitude. However, there is an important difference that simplifies the analysis of the O/C transition. Incident angles, j_1, for all rays trapped in and travelling through the oceanic crustal layer are greater than 51°. For $n > 1$ these angles increase. Therefore, no energy originally trapped in the oceanic crust is transmitted across the MCB, or reflected back towards the source.

Observations indicate that the length of the intermediate oceanic path between the C/O and O/C transitions is important. The results of this study suggest some reasons why this is so. For short paths energy transmitted into the mantle layer has little time to travel towards the bottom of the grid and thus out of the region of consideration before much of it passes back into the crustal layer in the O/C transition region. This implies that there may be a critical length of intermediate oceanic path beyond which enough of the energy has escaped from the region of interest that amplitudes of the attenuated L_g recorded after the O/C transition would be reduced sufficiently to explain the observed data. To completely analyse this assertion requires the use of the RT coupling method for continuing FE calculations through a plane-layered structure using RT integration and PM Green's functions. The accuracy of the numerical implementation of this method must be established before such calculations can be presented. Therefore, the discussion of the numerical implementation of this method and of the results examining the effects of the intermediate path length in the oceanic structure will be left for other papers.

CONCLUSIONS

This paper presents a discussion of the propagation of L_g along partially oceanic paths and the attenuation of L_g due to propagation through the transition regions between the continental and oceanic portions of these paths. The transition regions are modelled by a crustal layer with smoothly varying thickness which connects the continental and oceanic structures. The results will be discussed in three parts. First, propagation through the transition from continental to oceanic structure. Then, propagation through the oceanic structure and, finally, propagation through the transition from oceanic to continental structure.

The effects produced when a SH L_g mode sum wavefield is propagated through a continent to ocean (C/O) transition region, and their dependence on the horizontal extent of that transition region, L, will now be summarized. Amplitudes at the surface of the crust and in the crust are amplified by as much as 50 per cent as the wavefield passes through the transition region from the continental structure to the oceanic structure. These amplitude increases in the crustal layer have been explained by the increased ray density in the thinning crustal layer. The amount of amplification increases as L increases. Increased numbers of reflections within a longer transition region, cause an increase in ray density, explaining the increase in energy as L increases. Amplification is maximum at the surface and decreases with depth until the base of the oceanic crust is reached. In the transition region energy is transmitted across the boundary between the crustal layer and the mantle layer (the CMB) but not across the boundary between the crustal layer and the ocean layer (the COB). Thus, the amplification is maximum at the COB and decays as the CMB is approached and the effects of energy transmitted across the CMB increase. The amount of energy transmitted across the CMB increases as L increases. The translation

direction of the forward transmitted wavefield has a larger vertical component later in the seismogram when it approaches the normal to the CMB. Thus, for a longer transition, with a smaller ϕ_{cm} and thus a more horizontal CMB, the path length in the oceanic structure will have a larger vertical component. This will allow the transmitted energy to escape the system more readily as L increases.

After the wavefield has travelled through the transition region it travels through a region of oceanic structure. While travelling in this oceanic region additional energy escapes from the crustal layer. This leakage is largest near the end of the transition region and decreases with distance away from it. The size of the decrease in amplitude is controlled by the energy in wavefronts propagating through the oceanic crustal layer with pre-critical angles of incidence. At each successive reflection of such a wavefront at the crust half-space interface in the oceanic structure, a fraction of the total amplitude remaining, $T(j_{oc})$ is transmitted across the interface. Thus, the total amplitude of this component decays most rapidly in the first kilometres of the oceanic structure while the incident wave still has significant amplitudes.

After propagating through the oceanic region, the wavefield propagates through an ocean to continent (O/C) transition region. As the wavefield travels through the O/C transition region the surface amplitude decreases rapidly. The energy forming the concentrations of amplitude previously trapped in the oceanic crustal layer travels up the boundary between the oceanic and crustal layers (OCB) in the transition region while spreading throughout the depth extent of the crustal layer. The maxima in these regions remain at the surface. The amplitude decreases rapidly with depth down to the crust–mantle interface. The amplitude incident upon the boundary between the mantle layer and the crustal layer (MCB) in the O/C transition region from the oceanic half-space is transmitted across it with a resulting distortion in the wavefield. The form of this distortion is the superposition of a slope,

$$\text{Slope} = \tan^{-1}\left[\frac{l(v_M - v_c)}{v_M}\right],$$

on to the disturbance incident at the MCB after it has passed into the continental crustal layer.

Finally, attenuation of L_g propagating along a mixed path with simple transition regions and an oceanic path length of 147 km, is not sufficient to explain the observed values. The highest attenuations observed produced a reduction of a factor of two to three in amplitude. Observations of the trends due to varying L indicate that a longer C/O transition could increase the attenuation. But, even using the optimal L attenuation of more than a factor of four would not be expected. Thus, other factors and/or more complex structures must be considered to explain the observed attenuation of L_g along mixed paths.

ACKNOWLEDGMENTS

J. Regan conducted part of this research while a Canadian Government Laboratory Visiting Fellow at Geophysics Division, Geological Survey of Canada, Ottawa. This research was supported in part by the Advanced Research Projects Agency of the US Department of Defense and was monitored by the US Air Force Geophysics Laboratory under contract F19628-87-K-0028; Division of Geological Sciences Contribution No. 4623; Geological Survey of Canada Contribution No. 20988.

REFERENCES

Alsop, L. E., 1966. Transmission and reflection of Love waves at a vertical discontinuity, *J. geophys. Res.*, **71,** 3969–3984.

Barker, B., W., Der, Z. A., Mrazek, C. P., 1981. The effect of crustal structure on the regional phases P_g and L_g at the Nevada test site, *J. geophys. Res.*, **86,** 1686–1700.

Bath, M., 1954. The elastic waves L_g and R_g along Euroasiatic paths, *Arkiv Geofysik*, **2,** 295–342.

Blandford, R., 1982. Seismic event discrimination, *Bull. seism. Soc. Am.*, **72,** s69–s87.

Bolt, B. A., 1957. Velocity of the seismic waves L_g and R_g across Australia, *Nature*, **180,** 495.

Bollinger, G. A., 1979. Attenuation of the L_g phases and determination of m_b in the southeastern United States, *Bull. seism. Soc. Am.*, **69,** 45–63.

Boore, D., 1970. Love waves in nonuniform wave guides: finite difference calculations, *J. geophys. Res.*, **75,** 1512–1527.

Bose, S. K., 1975. Transmission of SH waves across a rectangular step, *Bull. seism. Soc. Am.*, **65,** 1779–1786.

Bouchon, M., 1981. A simple method to calculate Green's functions for elastic layered media, *Bull. seism. Soc. Am.*, **71,** 959–971.

Bouchon, M., 1982. The complete synthesis of seismic crustal phases at regional distances, *J. geophys. Res.*, **87,** 1735–1741.

Campillo, M., Bouchon, M. & Massinon, B., 1984. Theoretical study of the excitation, spectral characteristics, and geometrical attenuation of regional seismic phases, *Bull. seism. Soc. Am.*, **74,** 79–90.

Chung, D. H. & Bernreuter, D. L., 1981. Regional relationships among earthquake magnitude scales, *Rev. geophys. Space Phys.*, **19,** 649–663.

Drake, L. A., 1972. Love and Rayleigh waves in nonhorizontally layered media, *Bull. Seism. Soc. Am.*, **62,** 1241–1258.

Drake, L. A. & Bolt, B. A., 1980. Love waves normally incident at a continental boundary, *Bull. seism. Soc. Am.*, **70,** 1103–1123.

Dwyer, J. J., Herrmann, R. B. & Nuttli, O. W. 1983. Spatial attenuation of the L_g wave in the central United States, *Bull. seism. Soc. Am.*, **73,** 781–796.

Eittreim, S. & Grantz, A., 1979. CDP seismic sections of the western Beaufort continental margin, *Tectonophysics*, **59,** 251–262.

Frazier, G. A., Alexander, J. H. & Petersen, C. M., 1973. 3-D seismic code for the ILLIAC IV. *Systems, Science and Software Report Report SSS-R-73-1506.*

Gregersen, S., 1978. Possible mode conversion between Love and Rayleign waves at a continental margin, *Geophys. J. R. astr. Soc.*, **54,** 121–127.

Gregersen, S., 1984. L_g wave propagation and crustal structure differences near Denmark and North Sea, *Geophys. J. R. astr. Soc.*, **79,** 217–234.

Gregersen, S. & Alsop, L. E., 1974. Amplitudes of horizontally refracted Love waves, *Bull. seism. Soc. Am.*, **64,** 535–553.

Gregersen, S. & Alsop, L. E., 1976. Mode conversion of Love waves at a continental margin, *Bull. seism. Soc. Am.*, **66,** 1855–1872.

Harkrider, D. G., 1964. Surface waves in multilayered media, Part I. Rayleigh and Love waves from buried sources in a multilayered elastic half-space *Bull. seism. Soc. Am.*, **54,** 627–679.

Harkrider, D. G., 1970. Surface waves in multilayered elastic media, Part II. Higher mode spectra and spectral ratios from point sources in plane layered earth models, *Bull. seism. Soc. Am.*, **60,** 1937–1987.

Harkrider, D. G., 1981. Coupling near source phenomena into surface wave generation, in *Identification of Seismic Sources—Earthquake or Underground Explosion,* pp. 277–326, eds Husebye, E. S. & Mykkeltveit, S., Reidel, Dordrecht.

Herrin, E. E. & Minton, P. D., 1960. The velocity of L_g in the southwestern United States and Mexico, *Bull. seism. Soc. Am.*, **50,** 35–44.

Herrmann, R. B. & Kijko, A., 1983. Short period L_g magnitudes: instrument, attenuation, and source effects, *Bull. seism. Soc. Am.*, **73,** 1835–1850.

Herrmann, R. B. & Nuttli, O. W., 1975. Ground motion modelling at regional distances for earthquakes in a continental interior, II. Effect of focal depth, azimuth, and attenuation, *Int. J. Earthq. Eng Struct. Dyn.*, **4,** 59–77.

Herrmann, R. B. & Nuttli, O. W., 1982. Magnitude: the relation of M_L to m_{bL_g}, *Bull. seism. Soc. Am.*, **72,** 389–397.

Hinz, K., Schluter, H.-U., Grant, A. C., Srivastava, S. P., Unpleby, D. & Woodside, J., 1979. Geophysical transects of the Labrador Sea: Labrador to southwest Greenland, *Tectonophysics*, **59,** 151–183.

de Hoop, A. T., 1958. Representation theorems for the displacement in an elastic solid and their application to elastodynamic diffraction theory, *ScD Thesis,* Technische Hogeschool, Delft.

Hudson, J. A., 1977. The passage of elastic waves through an anomalous region—IV. Transmission of Love waves through a laterally varying structure, *Geophys. J. R. astr. Soc.*, **49,** 645–654.

Hudson, J. A. & Knopoff, L., 1964. Transmission and reflection of surface waves at a corner: I. Love waves, *J. geophys. Res.*, **69,** 275–280.

Jones, F. B., Long, L. T. & McKee, J. H., 1977. Study of the attenuation and azimuthal dependence of seismic wave propagation in the southeastern United States, *Bull. seism. Soc. Am.*, **67,** 1503–1513.

Kazi, M. H., 1978a. The Love wave scattering matrix for a continental margin (theoretical), *Geophys. J. R. astr. Soc.*, **52,** 25–44.

Kazi, M. H., 1978b. The Love wave scattering matrix for a continental margin (numerical), *Geophys. J. R. astr. Soc.*, **53,** 227–243.

Keen, C. E. & Hyndman, R. D. 1979. Geophysical review of the continental margins of eastern and western Canada, *Can. J. Earth Sci.*, **16,** 712–747.

Kennett, B. L. N., 1973. The interaction of seismic waves with horizontal velocity contrasts, *Geophys. J. R. astr. Soc.*, **33,** 431–450.

Kennett, B. L. N. & Mykkeltveit, S., 1984. Guided wave propagation in laterally varying media—II. L_g-waves in north-western Europe, *Geophys. J. R. astr. Soc.*, **79,** 257–267.

Kennett, B. L. N., 1986. L_g waves and structural boundaries, *Bull. seism. Soc. Am.*, **76,** 1133–1142.

Knopoff, L. & Hudson, J. A., 1964. Transmission of Love waves past a continental margin, *J. geophys. Res.*, **69,** 1649–1653.

Knopoff, L. & Mal, A. K., 1967. Phase velocities of surface waves in the transition zone of continental margins—I. Love waves, *J. geophys. Res.*, **72,** 1769–1776.

Knopoff, L., Mal, A. K., Alsop, L. E. & Phinney, R. A., 1970. A property of long-period Love waves, *J. geophys. Res.*, **75,** 4084–4086.

Knopoff, L., Schwab, F., Nakanishi, K. & Chang, F., 1975. Evaluation of L_g as a discriminant among different continental crustal structures, *Geophys. J. R. astr. Soc.*, **39,** 41–70.

Knopoff, L., Schwab, F. & Kausel, E., 1973. Interpretation of L_g, *Geophys. J. R. astr. Soc.*, **33,** 389–404.

Kovach, R. L. & Anderson, D. L., 1964. Higher mode surface waves and their bearing on the structure of the Earth's mantle, *Bull. seism. Soc. Am.*, **54,** 161–182.

Le Douaran, S., Burrus, J. & Avedik, F., 1984. Deep structure of the north-western Mediterranean basin: results of a two-ship survey, *Mar. Geol.*, **55,** 325–345.

Lehmann, I., 1952. On short period surface wave L_g and crustal structures, *Bull. D'information L'UGGI 2^e Aneé,* 248–251.

Lehmann, I., 1957. On L_g as read in North American records, *Ann. Geofis.*, **10,** 1–28.

Lysmer, J. & Drake, L. A., 1971. The propagation of Love waves across nonhorizontally layered structures, *Bull. seism. Soc. Am.*, **61,** 1233–1251.

Lysmer, J. & Drake, L. A., 1972. A finite element method for seismology, in *Methods in Computational Physics 11, Seismology,* Alder, B., Fernbach, S. & Bolt, B. A., Academic Press, New York.

Martel, L., 1980. Love wave propagation across a step by finite elements and spatial filtering, *Geophys. J. R. astr. Soc.*, **61,** 639–677.

Mantovani, E., Schwab, F., Liao, H. & Knopoff, L., 1977. Generation of complete theoretical seismograms for SH–II, *Geophys. J. R. astr. Soc.*, **48,** 531–535.

Nicolas, M., Massinon, B., Mechler, P. & Bouchon, M., 1982. Attenuation of regional phases in western Europe, *Bull. seism. Soc. Am.*, **72,** 2089–2106.

Nuttli, O. W., 1973. Seismic wave attenuation and magnitude relations for eastern North America, *J. geophys. Res.*, **78,** 876–885.

Nuttli, O. W., 1978. A time domain study of the attenuation of 10-Hz waves in the new Madrid seismic zone, *Bull. seism. Soc. Am.*, **68,** 343–355.

Nuttli, O. W., 1981. On the attenuation of L_g waves in western and central Asia and their use as a discriminant between earthquakes and explosions, *Bull. seism. Soc. Am.*, **71,** 249–261.

Oliver, J., Dorman, J. & Sutton, G., 1959. The second shear mode of continental Rayleigh waves, *Bull. seism. Soc. Am.*, **49,** 379–389.

Oliver, J., Ewing, M. & Press, F., 1955. Crustal structure of the Arctic regions from the L_g phase, *Bull. seism. Soc. Am.*, **66,** 1063–1074.

Oliver, J. & Ewing, M., 1957. Higher modes of continental Rayleigh waves, *Bull. seism. Soc. Am.*, **47,** 187–204.

Oliver, J. & Ewing, M., 1958. Normal modes of continental surface waves, *Bull. seism. Soc. Am.*, **48,** 33–49.

Panza, G. F. & Calcagnile, G., 1974. Comparison of multimode surface wave response in structures with and without a low velocity channel (Part I: Dip slip sources on a vertical fault plane), *Pure appl. Geophys.*, **112,** 583–596.

Panza, G. F. & Calcagnile, G., 1975. L_g, L_i and R_g from Rayleigh modes, *Geophys. J. R. astr. Soc.*, **40,** 475–487.

Pec, K., 1967. Theoretical dispersion tables for Love waves propagating in a wedge and in a single nonhomogeneous layer with a linear velocity gradient, *Pub. Dominion Obs. Ottawa,* **35.**

Pomeroy, P. W., Best, W. J. & McKevilly, T. V. 1982. Test ban treaty verification with regional data: a review, *Bull. seism. Soc. Am.*, **72,** s89–s129.

Press, F., 1956. Velocity of L_g waves in California, *Trans. Am. geophys. Un.*, **37,** 615–618.

Press, F. & Ewing, M., 1952. Two slow surface waves across North America, *Bull. seism. Soc. Am.*, **42,** 219–228.

Press, F., Ewing, M. & Oliver, J., 1956. Crustal structure and surface-wave dispersion in Africa, *Bull. seism. Soc. Am.*, **46,** 97–103.

Regan, J., 1987. Numerical studies of propagation of L_g waves across ocean continent boundaries using the representation theorem, *PhD thesis,* California Institute of Technology, Pasadena, Ca.

Sato, R., 1961a. Love waves propagated across transitional zone, *Japan. J. Geophys.*, **2,** 117–134.

Sato, R., 1961b. Love waves in case the surface layer is variable in thickness, *J. Phys. Earth.*, **9,** 19–36.

Savarensky, E. & Valdener, N., 1960. Observations of L_g and R_g waves from the Black Sea basin earthquakes, *Ann. Geofis.*, **13,** 129–134.

Schwab, F., Kausel, E. & Knopoff, L., 1974. Interpretation of S_a for a shield structure, *Geophys. J. R. astr. Soc.*, **36,** 737–742.

Singh, S. & Herrmann, R. B., 1983. Regionalization of crustal coda Q in the continental United States, *J. geophys. Res.*, **88,** 527–538.

Stephens, C. & Isacks, B. L., 1977. Toward an understanding of S_n: normal modes of Love waves in an oceanic structure, *Bull. seism. Soc. Am.*, **67,** 69–78.

Street, R., 1976. Scaling northeastern United States/southeastern Canadian earthquakes by their L_g waves, *Bull. seism. Soc. Am.*, **66,** 1525–1537.

Street, R., 1984. Some recent L_g phase displacement spectral

densities and their implications with respect to the prediction of ground motions in eastern North America, *Bull. seism. Soc. Am.*, **74,** 757–762.

Street, R., Herrmann, R. B. & Nuttli, O. W., 1975. Spectral characteristics of the L_g wave generated by central United States earthquakes *Geophys. J. R. astr. Soc.*, **41,** 51–63.

Street, R. & Turcotte, F. T., 1977. A study of northeastern North American spectral moments, magnitudes, and intensities, *Bull. seism. Soc. Am.*, **67,** 599–614.

Wetmiller, R. J., 1974. Crustal structure of Baffin Bay from earthquake generated L_g phases, *Can. J. Earth Sci.*, **11,** 123–130.

Zienkiewicz, O. C. & Cheung, Y., 1967. *The Finite Element Method in Structural and Continuum Mechanics,* McGraw-Hill.